Interpreting radial correlation Doppler reflectometry using gyrokinetic simulations

To cite this article: J Ruiz Ruiz *et al* 2022 *Plasma Phys. Control. Fusion* **64** 055019

OPEN ACCESS
IOP Publishing
Plasma Physics and Controlled Fusion
Plasma Phys. Control. Fusion **64** (2022) 055019 (25pp)
https://doi.org/10.1088/1361-6587/ac5916

Interpreting radial correlation Doppler reflectometry using gyrokinetic simulations

J Ruiz Ruiz[1,*], F I Parra[1], V H Hall-Chen[1], N Christen[1], M Barnes[1], J Candy[2], J Garcia[3], C Giroud[4], W Guttenfelder[5], J C Hillesheim[4], C Holland[6], N T Howard[7], Y Ren[5], A E White[7] and JET contributors[8]

[1] Rudolf Peierls Centre for Theoretical Physics, University of Oxford, Oxford OX1 3NP, United Kingdom
[2] General Atomics, PO Box 85608, San Diego, CA, United States of America
[3] CEA, IRFM, F-13108 Saint-Paul-lez-Durance, France
[4] CCFE, Culham Science Centre, Abingdon, Oxon OX14 3DB, United Kingdom
[5] Princeton Plasma Physics Laboratory, Princeton, NJ 08543, United States of America
[6] Center for Energy Research, University of California, San Diego, 9500 Gilman Drive, La Jolla, CA 92093-0417, United States of America
[7] MIT-Plasma Science and Fusion Center, Cambridge, MA 02139, United States of America

E-mail: juan.ruiz@physics.ox.ac.uk

Received 5 August 2021, revised 28 January 2022
Accepted for publication 28 February 2022
Published 12 April 2022

Abstract

A linear response, local model for the DBS amplitude applied to gyrokinetic simulations shows that radial correlation Doppler reflectometry measurements (RCDR, Schirmer *et al* 2007 *Plasma Phys. Control. Fusion* **49** 1019) are not sensitive to the average turbulence radial correlation length, but to a correlation length that depends on the binormal wavenumber $k_\perp$ selected by the Doppler backscattering (DBS) signal. Nonlinear gyrokinetic simulations show that the turbulence naturally exhibits a nonseparable power law spectrum in wavenumber space, leading to a power law dependence of the radial correlation length with binormal wavenumber $l_r \sim Ck_\perp^{-\alpha} (\alpha \approx 1)$ which agrees with the inverse proportionality relationship between the measured l_r and $k_\perp$ observed in experiments (Fernández-Marina *et al* 2014 *Nucl. Fusion* **54** 072001). This new insight indicates that RCDR characterizes the eddy aspect ratio in the perpendicular plane to the magnetic field. It also motivates future use of a nonseparable turbulent spectrum to quantitatively interpret RCDR and potentially other turbulence diagnostics. The radial correlation length is only measurable when the radial resolution at the cutoff location W_n satisfies $W_\mathrm{n} \ll l_r$, while the measurement becomes dominated by W_n for $W_\mathrm{n} \gg l_r$. This suggests that l_r is likely to be inaccessible for electron-scale DBS measurements ($k_\perp \rho_\mathrm{s} > 1$). The effect of W_n on ion-scale radial correlation lengths could be nonnegligible.

[8] See the author list of 'Overview of JET results for optimising ITER operation' by J Mailloux *et al* to be published in *Nuclear Fusion Special issue: Overview and Summary Papers from the 28th Fusion Energy Conference (Nice, France, 10–15 May 2021)*.

* Author to whom any correspondence should be addressed.

Keywords: Doppler backscattering, synthetic diagnostics, gyrokinetic simulation, radial correlation Doppler reflectometry, turbulent correlation length

(Some figures may appear in colour only in the online journal)

1. Introduction

Decades of development in fusion energy research have provided strong experimental evidence [1, 2] and theoretical support [3, 4] for microscale turbulent fluctuations being ultimately responsible for driving anomalous transport in the core of magnetic confinement devices. The turbulence is driven by the large density and temperature gradients in the tokamak core, which provide free energy to drive microscale instabilities that ultimately develop into turbulence. First-principles nonlinear gyrokinetic simulations of the turbulence have routinely been successful at predicting the experimental levels of anomalous transport in some plasma scenarios [5]. These numerical and theoretical studies yield an understanding of the turbulent processes, but can only provide indirect evidence of the turbulence. The most definitive experimental evidence can be provided by fluctuation diagnostics, which measure fluctuations in density, temperature, magnetic field and flows that are produced by the turbulence. Making quantitative interpretations of the fluctuation measurements has proven to be a great challenge for the validation of existing turbulence and transport models [6–8]. The highly sophisticated nature of the measurement process has motivated the development of synthetic diagnostics to understand not only the turbulent fluctuations, but also the measurement process taking place in fluctuation measurements.

The radial correlation length is an important intrinsic characteristic of the turbulence with a direct relation to transport. Several diagnostics have been successful at measuring turbulence radial correlation lengths in the core plasma, such as beam emission spectroscopy (BES [9–11]), phase-contrast imaging/interferometry [12–16], correlation electron cyclotron emission [17–19] and radial correlation reflectometry (RCR [20–24]). Measurements using radial correlation reflectometry have proven particularly challenging to interpret, often yielding unphysically large or small values [23, 25–30]. In the literature, the unusually short correlation lengths are often attributed to the nonlinear response of the reflectometer to the density fluctuation amplitude [31], while the unusually large values have mostly been attributed to the presence of a small angle forward-scattering contribution due to long radial scale turbulent fluctuations [32].

A more recent evolution of radial correlation reflectometry is radial correlation Doppler reflectometry (RCDR [33]), implemented via radial correlation of Doppler backscattering signals. Doppler backscattering [34, 35] is a standard and versatile diagnostic capable of measuring the turbulent wavenumber spectrum [36, 37], zonal and equilibrium flows [38–40], as well as the turbulent correlation length [33]. As in standard reflectometry, the Doppler backscattering technique launches a microwave beam into the core plasma, but with a finite incidence angle with respect to the horizontal. The beam propagates in the plasma until it encounters a cutoff surface, where the forward beam is refracted away from the detector and only the backscattering contribution is collected. This scheme is believed to remove, or greatly reduce, the small angle forward scattering contribution to the radial correlation in the linear regime [41, 42] that hinders standard reflectometry. The finite incidence beam launch angle makes the backscattered signal sensitive to a specific turbulence wavenumber $\mathbf{k}_\perp$ that is selected by the scattering process, which is related to the central ray wave-vector value $\mathbf{k}_i$ (taken at the cutoff location) by the Bragg condition for backscattering at the cutoff $\mathbf{k}_\perp = -2\mathbf{k}_i$ [34, 35] ($\mathbf{k}_i$ is a function of the incident beam launch angle).

Experiments measuring the radial correlation length via the RCDR technique have provided radial correlation lengths characteristic of ion-scale eddies $l_r \approx 3$–$10\ \rho_\mathrm{s}$ [33, 43–48, 109], which are more consistent with theory than its reflectometer counterpart ($\rho_\mathrm{s} = c_\mathrm{s}/\omega_\mathrm{ci}$ is the ion-sound gyro-radius computed using the local toroidal field $B = |\mathbf{B}_\varphi|$ and electron temperature T_e, $c_\mathrm{s} = \sqrt{T_\mathrm{e}/m_\mathrm{i}}$ is the sound speed, $\omega_\mathrm{ci} = eB/m_\mathrm{i}c$ is the gyro-frequency, m_i is the main ion mass, e is the proton charge and c the speed of light). However, open questions still remain about the interpretation of the measured values. The 'common wisdom' is that experimentally-relevant values of the selected $k_\perp$ by DBS lie on the intermediate to electron-scale range, that is $k_\perp\rho_\mathrm{s} \gtrsim 1$. This would imply that the fluctuations measured by DBS are in fact intermediate-to-electron scales in the binormal $k_\perp$ direction, but exhibit radial correlation lengths that are of the order of the ion gyroradius. Part of the present work seeks to clarify the origin of this result of DBS measurements.

Careful analysis of DBS systems in different magnetic confinement devices shows that disparate values of $k_\perp$ are accessible via DBS, ranging from electron to ion scales, as shown in figure 1. The measured $k_\perp\rho_\mathrm{s}$ is shown to scale closely with the local value of electron beta to the $1/2$ power, $k_\perp\rho_\mathrm{s} \propto \beta_e^{0.5}$, which can be explained as follows. Due to the backscattering Bragg condition, the measured $k_\perp$ scales with the incident k_i of the microwave beam $k_\perp\rho_\mathrm{s} \sim k_i\rho_\mathrm{s}$. In turn, the incident k_i is related to the frequency of the cutoff surface ω due to the cutoff condition, that is $k_i \sim \omega/c$. To simplify the argument, we assume $\omega \approx \omega_{pe}$ the electron plasma frequency (strictly valid for normal incidence, O-mode polarization). Thus, $k_\perp\rho_\mathrm{s} \sim \omega_{pe}\rho_\mathrm{s}/c$, which is rewritten as $k_\perp\rho_\mathrm{s} \sim (m_D/m_e)^{0.5}\beta_e^{0.5}$ for a deuterium plasma. Although seemingly simplistic, this relationship between the selected $k_\perp\rho_s$ and the local value of β_e is shown to perform fairly satisfactorily when contrasted with DBS measurements from different machines in figure 1. Figure 1 is constructed using values of $k_\perp\rho_s$ and

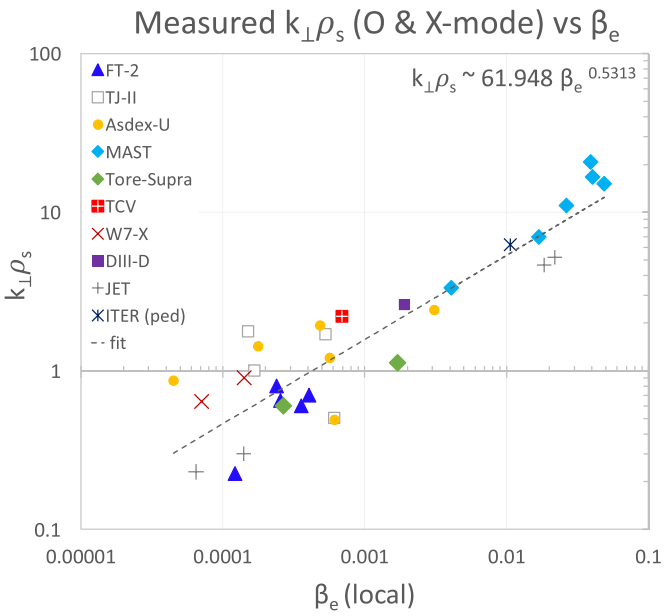

Figure 1. Measured $k_\perp \rho_s$ from a series of magnetic confinement devices vs. the local values of β_e [33, 37, 40, 43–46, 49–59, 109]. The scaling of $k_\perp \rho_s$ with β_e can be explained by the Bragg condition for scattering and the cutoff condition, yielding $k_\perp \rho_s \sim (m_D/m_e)^{0.5} \beta_e^{0.5}$ (O-mode). In plasma regimes characterized by low β_e ($\beta_e \approx 10^{-5}$–10^{-4} at the pedestal, high-field machines or low performance discharges) DBS will predominantly measure ion-scale wavenumbers $k_\perp \rho_s < 1$, while in high β_e scenarios ($\beta_e \approx 10^{-2}$–10^{-1} in high performance regimes or spherical tokamaks), it will likely be sensitive to intermediate to electron-scales $k_\perp \rho_s \gtrsim 1$. ITER values correspond to pedestal projections from [59]. The figure is not an accurate representation of the measurement capabilities of specific devices, but indicative of the measured $k_\perp \rho_s$ for a specific value of β_e.

β_e that are either provided or computed using alternate quantities provided in [33, 37, 40, 43–46, 49–59, 109]. There is natural scatter in the values. There are likely errors in the measurement and in the computation of $k_\perp \rho_s$ and β_e. Perhaps more importantly, this scaling does not take into account the dependence on the incident launch angle of the microwave beam in a specific scattering experiment, which can admittedly yield differences in the order of ∼1–10 in the measured $k_\perp$. However, when spanning four orders of magnitude in β_e, these important factors appear not to have a dramatic effect on this scaling, as suggested by a least-squares power law fit $k_\perp \rho_s \sim 61.95\ \beta_e^{0.53}$, which remains close to the naive scaling $k_\perp \rho_s \sim (m_D/m_e)^{0.5} \beta_e^{0.5}$ presented.

This dimensionless scaling is *not* an equality relating $k_\perp \rho_s$, $(m_D/m_e)^{0.5}$ and β_e. Figure 1 does *not* represent the measured $k_\perp$ range achievable by a specific machine (except possibly the range reported for JET[9]). However, when looking at the global range of DBS measurements and not at specific plasma conditions or machines, figure 1 shows that DBS measurements taking place in low β_e plasma regimes ($\beta_e \approx 10^{-5}$–10^{-4}) will likely be sensitive to ion-scale wavenumbers $k_\perp \rho_s < 1$ (at the pedestal, high-field machines or low performance discharges), while high β_e scenarios ($\beta_e \approx 10^{-2}$–10^{-1} as in high performance regimes or spherical tokamaks) will likely be sensitive to intermediate to electron scales $k_\perp \rho_s \gtrsim 1$. This confirms that DBS measurements can in fact be sensitive to ion- and electron-scale wavenumbers $k_\perp$, and motivates the separate study of ion- vs. electron-scale turbulence, and their differing implications on radial correlation length measurements via RCDR.

In this work, we seek to discover: the dependence of the radial correlation length on the measured $k_\perp$, and the potential diagnostic resolution effects on radial correlation length measurements via RCDR in the linear response regime [41, 60, 61]. The rest of this manuscript proceeds as follows. Section 2 describes the modelling approach employed. We use nonlinear gyrokinetic simulations and a synthetic model DBS developed for gyrokinetic simulations. In section 3 we study the synthetic and average radial correlation lengths l_r of electron-scale turbulent fluctuations computed from a strongly-driven ETG regime in the NSTX core [63–66, 69] using the GYRO code [67, 70]. In section 4 we carry out a parallel study of the synthetic and average radial correlation lengths l_r of ion-scale turbulent fluctuations computed from a fully developed ITG-driven turbulence regime in the JET core [71, 72] using the GS2 code [68]. In section 5 we discuss the implication of employing separable turbulence spectra to model the DBS response. We conclude in section 6.

2. Modelling approach

In this section, we describe the modelling approach developed to calculate synthetic RCDR correlation lengths from simulated turbulence output from nonlinear gyrokinetic simulations. We also present the description of a model DBS suitable for filtering the density fluctuation field from gyrokinetic simulations.

2.1. Gyrokinetic simulations and wavenumber definitions

Owing to the disparate wavenumber range accessible by DBS measurements (figure 1), we analyze two different plasma turbulence conditions: a highly unstable ETG turbulence regime ($k_\perp \rho_s > 1$) in the outer core of a modest-beta NSTX NBI heated H-mode (section 3, analyzed in [63–66]), and a fully developed ITG turbulence regime ($k_\perp \rho_s < 1$) from the mid-core of a JET NBI heated L-mode plasma (section 4, [71, 72]). Seeking generality in the approach, we have implemented and deployed a model DBS valid for both nonlinear gyrokinetic simulations from the GYRO code [67, 70] corresponding to the NSTX ETG regime, and GS2 [68] simulations for the JET ITG regime.

Local, nonlinear gyrokinetic simulations from GYRO and GS2 solve the nonlinear, gyrokinetic equation [73] in the local limit ($\rho_s/a \to 0$), where a is the plasma minor radius. While GYRO and GS2 use different definitions for the reference magnetic field (B_{unit} [67, 70] for GYRO and B_{ref}

[9] Low β_e values for JET are from low performance edge measurements [40, 57, 58], while the high β_e values are taken from the inner core of reference discharges 94 042 and 95 274 ($\Psi_N \approx 0.1$–0.2, $\beta_N \approx 1.8$).

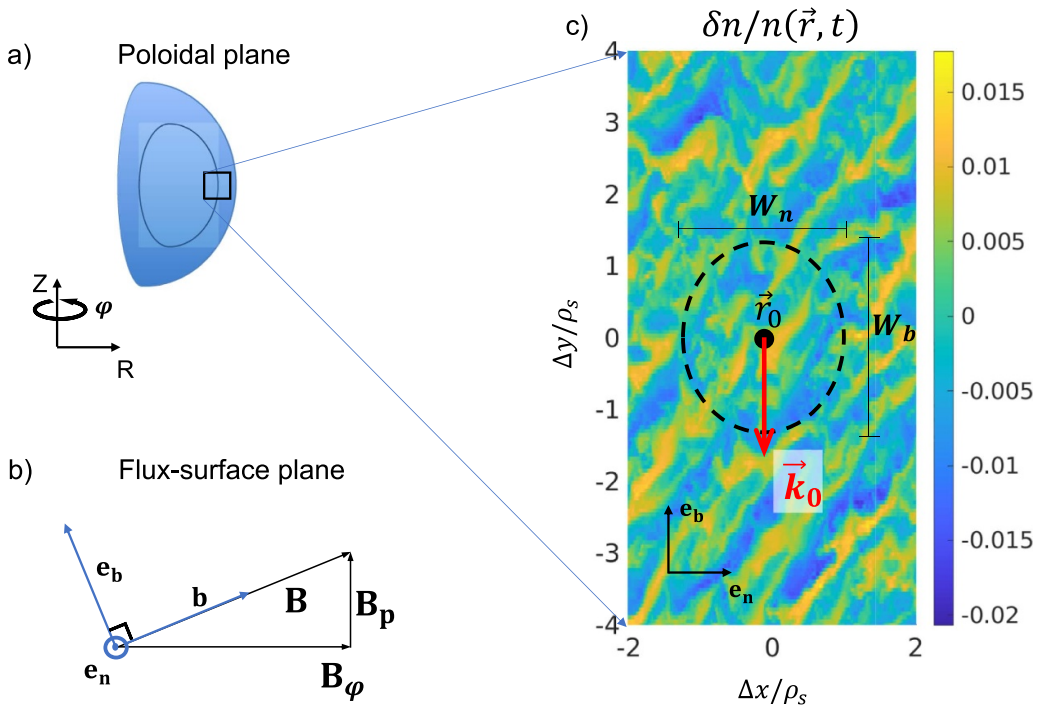

Figure 2. Schematic representation of the model DBS. (a) Poloidal plane cross section. (b) Flux-surface plane showing the orthonormal vectors **b** along **B**, normal direction $\mathbf{e_n}$ and binormal $\mathbf{e_b}$. $\mathbf{B}_\varphi$ and $\mathbf{B_p}$ are the toroidal and poloidal magnetic field directions, schematically shown for reference. (c) Density fluctuation field δn plotted in terms of real-space perpendicular directions $\mathbf{e_n}$ and binormal $\mathbf{e_b}$. W_n and W_b are the filter characteristic length scales along $\mathbf{e_n}$ and $\mathbf{e_b}$ ($W_b \gg 2\pi/k_{b0}$). The lengths in figure (c) are lengths as would be viewed by an external observer. Accordingly, ρ_s is the ion-sound gyro-radius evaluated at the local toroidal field $B = |\mathbf{B}_\varphi|$.

for GS2, appendix A), in this manuscript the quoted ρ_s is computed using local toroidal magnetic field magnitude $B = |\mathbf{B}_\varphi|$ (figure 2(b)) and electron temperature T_e values at the outboard midplane (unless otherwise specified). The electron density fluctuation field δn calculated from nonlinear gyrokinetic simulations is used in this analysis to calculate the scattered amplitude and radial correlation lengths.

Both GYRO and GS2 use a field-aligned coordinate system in which the fluctuating field δn exhibits a slowly varying dependence along the field line, described by the coordinate θ, and rapidly varying components perpendicular to the field line, described by (x, y). Here x is the physical distance in the radial, normal direction to the flux surface, and y is in the binormal direction (on the flux surface and perpendicular to the magnetic field **B**). In this work, the coordinates (x, y) represent real lengths in the laboratory frame, and are transformed from the internal GYRO and GS2 coordinates perpendicular to **B** (resp. (k_r, k_θ) in GYRO, (k_x, k_y) in GS2, details in appendix A). In this manuscript, we restrict ourselves to fluctuations taken at the outboard midplane ($\theta = 0$), which is the location where traditional electrostatic drift-wave ballooning-type instabilities tend to exhibit the highest amplitude and where the vast majority of fluctuation measurements take place. Off-midplane locations might exhibit lower fluctuation amplitudes for ballooning instabilities, and tilted turbulent eddies in the perpendicular plane for finite magnetic shear. These effects are not considered here for simplicity. For the purpose of analyzing the electron density field δn that predominantly contributes to scattering, we decompose the perpendicular wave-vector into its normal and binormal components $\mathbf{k}_\perp = k_n \mathbf{e_n} + k_b \mathbf{e_b}$. Here we note the normal direction $\mathbf{e_n}$ as the perpendicular direction to the flux surface (x-direction), and the binormal direction $\mathbf{e_b}$ as the perpendicular direction to the magnetic field **B** and to $\mathbf{e_n}$ (y-direction), which lies in the flux surface (additional details in appendix A).

Given the wavenumber definitions for (k_n, k_b) [m^{-1}] and the physical space (x, y) [m], we use the expansion of the density fluctuation field $\delta n(x, y, \theta, t)$ typical of a local flux tube (applicable to GYRO and GS2 in particular), given by:

$$\delta n(x, y, \theta = 0, t) = \sum_{k_n, k_b} \delta \hat{n}(k_n, k_b, \theta = 0, t) \mathrm{e}^{ik_n x + ik_b y}. \quad (1)$$

Equation (1) states that (k_n, k_b) and (x, y) are simply Fourier conjugate variables (note the distinction between Euler number e and the electric charge e made throughout the manuscript). An example density fluctuation amplitude is given in figure 2(c).

The use of the (x, y) coordinates and the normal k_n and binormal k_b wavenumber components of $\mathbf{k}_\perp$ has two main motivations in this work. First, k_n and k_b [m^{-1}] are routinely provided in experimental measurements via ray-tracing or beam-tracing methods (at the cutoff location), and correspond to real inverse lengths in physical space (the difference between the binormal k_b and poloidal component of **k** might be small in conventional tokamak scenarios, but is substantial at the outboard midplane in spherical tokamak plasmas where the field-line pitch angle can reach $\sim 45°$). Correspondingly, (x, y)

[m] are real lengths in physical space. This should make the content of the present manuscript accessible for interpretation to the experimental plasma physicist and diagnostics expert. Secondly, the components k_n and k_b are independent of the internal wavenumber definitions in a specific gyrokinetic code. This makes k_n and k_b a general point of reference for synthetic diagnostics deployed in different gyrokinetic codes. In this manuscript, we assume a measurement at the outboard midplane, and we normalize k_n and k_b by the local value of the ion-sound gyro-radius, denoted ρ_s from now on, which is also independent of the reference magnetic field definitions used in gyrokinetic codes. For reference, ρ_s takes the value $\rho_s \approx 0.7$ cm in the NSTX ETG case, while $\rho_s \approx 0.33$ cm in the JET ITG case analyzed.

2.2. Model DBS

The model DBS implemented for gyrokinetic simulations can be derived from a first principles, linear response, beam-tracing DBS model developed by Hall-Chen *et al* [74], and is in line with previous synthetic DBS diagnostics implemented for GYRO [75–77]. In this work, our model assumes fixed wave polarization of the scattering process (O-mode or X-mode), beam localization modelled via a Gaussian filter (response localized to the cutoff), no scattering along the beam path ($k_n = 0$) and no mismatch angle between the binormal direction and the microwave beam wave-vector $\mathbf{k_i}$ [37, 74, 78]. The model is only applicable in the *linear* response regime [41, 60, 61] of the DBS reflectometer. The scattering amplitude is modelled by:

$$A_s(\mathbf{r_0},\mathbf{k}_0,t) = \int \mathrm{d}^3\mathbf{r}\ \delta n(\mathbf{r},t) U(\mathbf{r}-\mathbf{r_0}) \mathrm{e}^{-i\mathbf{k}_0\cdot\mathbf{r}} = \mathrm{e}^{-i\mathbf{k}_0\cdot\mathbf{r}_0} \sum_{\mathbf{k}_\perp} \delta\hat{n}(\mathbf{k}_\perp,\theta,t) W(\mathbf{k}_\perp - \mathbf{k}_0). \quad (2)$$

The function U is the filter in real space, while W is the filter in $\mathbf{k}$-space. These are related to each other via a Fourier transform. The sum $\sum_{\mathbf{k}_\perp}$ is made over the perpendicular wavenumbers k_n and k_b. The dot product $\mathbf{k_0}\cdot\mathbf{r} = k_{b0}y$ only exhibits a component in the binormal y-direction, emphasizing that no finite k_n corrections to the DBS signal are retained in the model. Here k_{b0} is the *measured* $k_\perp$ routinely quoted in experiments, modelling and simulation of Doppler backscattering. We take the filter U to have a Gaussian shape in the perpendicular directions (x, y), while no structure is given along the field line (expressions are evaluated at the outboard midplane $\theta = 0$). As a result, the filter W is also Gaussian in $\mathbf{k}$-space, namely:

$$U(\mathbf{r}-\mathbf{r_0}) = \frac{1}{\pi W_n W_b} \mathrm{e}^{-(x-x_0)^2/W_n^2} \mathrm{e}^{-(y-y_0)^2/W_b^2},$$

and

$$W(\mathbf{k}_\perp - \mathbf{k}_{\perp 0}) = \mathrm{e}^{ik_b y_0 + ik_n x_0} \mathrm{e}^{-(k_b-k_{b0})^2/\Delta k_b^2} \mathrm{e}^{-k_n^2/\Delta k_n^2}, \quad (3)$$

where (x_0, y_0) is the location of the scattering. The radial spot size W_n in the normal direction $\mathbf{e_n}$ is generally known as the radial resolution of the diagnostic. Its Gaussian shape is the result of assuming that the microwave field pattern is accurately represented by a Gaussian beam [74]. The Gaussian shape in y can be interpreted as the localization of the DBS signal at the cutoff location. As we will see, the specific shape of the filter U in the y-direction is unimportant in this work as long as $W_b \gg 2\pi/k_{b0}$, which is largely satisfied in all DBS experiments. The model also assumes a localized signal at the cutoff, that is, W_b is much smaller than a typical equilibrium length scale, which neglects scattering contributions along the beam path and is consistent with the selected wavenumber component $k_n = 0$. Δk_b is known as the wavenumber resolution of the diagnostic (commonly noted $\Delta k_\perp$ in the literature), and is related to the filter spot-size W_b at the cutoff via $\Delta k_b = 2/W_b$. The radial filter size W_n, or radial resolution, is related to the normal wavenumber resolution via $\Delta k_n = 2/W_n$. The radial resolution W_n includes a combination of the physical beam width and phase surface curvature.

For the purpose of studying the radial correlation properties of the turbulence via RCDR, we define three different cross-correlation functions (CCF):

$$\mathrm{CCF}^{\mathrm{avg}}(\Delta x) = \frac{\langle \delta n(x+\Delta x,y)\delta n(x,y)\rangle_{x_0,y_0,T}}{\langle|\delta n(x,y)|^2\rangle_{x_0,y_0,T}} = \text{Average turbulence CCF},$$

$$\mathrm{CCF}^{k_b}(\Delta x) = \frac{\langle \delta\tilde{n}(x+\Delta x,k_b)\delta\tilde{n}(x,k_b)^*\rangle_{x_0,T}}{\langle|\delta\hat{n}(x,k_b)|^2\rangle_{x_0,T}} = \text{Scale-dependent CCF for } k_b$$

$$\mathrm{CCF}^{\mathrm{syn}}(\Delta x) = \frac{\langle A_s(\mathbf{r_0}+\Delta x\,\mathbf{e_n},k_{b0}\mathbf{e_b})A_s(\mathbf{r_0},k_{b0}\mathbf{e_b})^*\rangle_{x_0,y_0,T}}{\langle|A_s(\mathbf{r_0},k_{b0}\mathbf{e_b})|^2\rangle_{x_0,y_0,T}} = \text{CCF of synthetic DBS}, \quad (4)$$

where the θ and t coordinates are omitted from δn for clarity (recall $\theta = 0$). The field $\delta\tilde{n}$ is Fourier transformed in y but not in x (appendix B). The subscripts $\langle.\rangle_{x_0,\ldots}$ denote the ensemble averaging performed in x_0, y_0 within the perpendicular simulation domain, and in time t during an interval T. Specifically, $\langle.\rangle_{x_0} = 1/L_x \int \mathrm{d}x_0(.)$, and equivalently

for y_0 and t (L_x is the simulation radial box-size). In what follows, we define the radial correlation length l_r by the $1/e$ value of the corresponding CCF.

We call the quantity $\mathrm{CCF}^{\mathrm{avg}}$ the *average* turbulence cross-correlation function, computed via radial correlation of the full density field δn from the gyrokinetic code for different radial separations Δx. As a result, $\mathrm{CCF}^{\mathrm{avg}}$ knows about the full turbulence spectrum. It is independent of any experimental factor and is intrinsic to the specific turbulence under consideration. The quantity CCF^{k_b} in equation (4) is the scale-dependent correlation function corresponding to a specific turbulence wavenumber k_b, and informs about the characteristic radial correlation of turbulent eddies with binormal wavenumber k_b. This quantity does not know about the full turbulence spectrum, but is intrinsic to k_b. This means that each binormal wavenumber k_b in the turbulence, or equivalently each binormal wavelength, has a specific radial structure associated with it, and it is given by CCF^{k_b}. CCF^{k_b} is *not* related to a diagnostic effect. In this manuscript, we argue that this is the quantity that can be measured via RCDR under the right conditions (when the resolution $W_n \ll l_r(k_{b0})$, where $l_r(k_{b0})$ is the radial correlation length of wavenumber k_{b0}). The last quantity in equation (4) is $\mathrm{CCF}^{\mathrm{syn}}$, the synthetic cross-correlation function, computed via radial correlation of the scattered amplitude A_s (equation (2)). Notably this cross-correlation function is directly dependent on specific experimental parameters, which in this model are k_{b0}, W_n and W_b (recall here $W_b \gg 2\pi/k_{b0}$). Part of the work that follows seeks to explain how the measured k_{b0} and W_n affect the synthetic cross-correlation function $\mathrm{CCF}^{\mathrm{syn}}$. This should prove highly useful for the interpretation of the radial correlation length measured via RCDR.

3. Interpreting l_r from electron-scale turbulence

In this section, we analyse the radial correlation properties of electron-scale turbulent fluctuations ($k_\perp \rho_s > 1$). A strongly-driven ETG regime is chosen to perform local, electron-scale nonlinear gyrokinetic simulations using the GYRO code. The simulations represent the outer-core ($r/a \approx 0.7$) of an NSTX NBI-heated H-mode plasma (NSTX discharge 141 767, $P_{NBI} \approx 2$ MW). This radial location has been the object of thorough analysis of turbulent transport and high-k density fluctuations in previous works [63–66, 69], where it was referred to as the 'strong ETG' regime. Ion thermal transport was close to neoclassical levels as computed by NEO [79] and subdominant to electron thermal transport, consistent with ion-scale turbulence being stabilized by strong $E \times B$ shear. Importantly, electron-scale simulations were shown to reproduce the experimental electron heat flux estimate computed via TRANSP [80], as well as the wavenumber spectrum shape and fluctuation level ratio [64], demonstrating the experimental relevance of the current ETG-driven turbulence simulations.

Simulations were performed at $r/a \approx 0.7$ (r is the minor radius coordinate normalized to the last closed flux surface value a), resolving three gyrokinetic species (e^-, D, C), including electron collisions ($\nu_{ei} \approx 1\ a/c_s$, but not ion collisions), background flow and flow shear (Mach number $M \approx 0.2$, $E \times B$ shearing rate $\gamma_E \approx 0.1$–$0.2\ a/c_s$, and parallel velocity gradient $\gamma_p \approx 1\ a/c_s$), and fully electromagnetic fluctuations including electrostatic potential $\delta\phi$, shear $\delta A_{||}$ and compressional $\delta B_{||}$ magnetic field perturbations. Linear background profiles were simulated employing nonperiodic boundary conditions in the radial direction with typical buffer widths $\Delta_b \approx 1\ \rho_{s,\mathrm{unit}}$. The simulation domain is characterized by radial and poloidal box sizes of dimensions $(L_r, L_\theta) \approx (7,7)\rho_{s,\mathrm{unit}}$, equating to radial and poloidal wavenumber resolutions $k_r\rho_{s,\mathrm{unit}} \in [0.9, 62]$, $k_\theta\rho_{s,\mathrm{unit}} \in [0.9, 65]$. Here, k_r and k_θ are the radial and poloidal wavenumbers internally defined in GYRO, which are related to k_n and k_b as shown in appendix A, and $\rho_{s,\mathrm{unit}}$ uses the GYRO internal B_{unit} definition ([67, 70], appendix A). Parallel resolution employed 14 poloidal grid points ($\times$ 2 signs of parallel velocity), 12 energies and 12 pitch-angles (6 passing + 6 trapped). This choice of numerical grids was made according to previous convergence and accuracy tests for the GYRO code simulating micro-instabilities in the core of NSTX [81], and were also tested for convergence in the present conditions [64]. The flux surface geometry is described by a Miller equilibrium [82].

3.1. Scale-dependent, physical correlation length

Before applying the model DBS to gyrokinetic simulations, we discuss some important correlation properties in the electron-scale turbulence by analyzing the 'raw' electron density fluctuating field δn output from the gyrokinetic simulation. We start by considering the case where the background $E \times B$ shear is 0 ($\gamma_E = 0$, shown in figures 3(a) and (b)). Figure 3(a) shows the average turbulence radial correlation function $\mathrm{CCF}^{\mathrm{avg}}$ (black empty circles) overlaid on a series of scale-dependent correlation functions CCF^{k_b} corresponding to different wavenumbers $k_b\rho_s = 3.22, 6.43, 13.67, 20.1$, computed using the definitions from equation (4). The radial correlation function corresponding to each individual k_b is different from the average turbulence correlation function, and it becomes wider for smaller k_b. This indicates that smaller turbulent k_b (larger eddies in the y direction) exhibit wider radial correlation functions, that is, larger radial correlation lengths. This can be more quantitatively assessed in figure 3(b).

Figure 3(b) shows the scale-dependent radial correlation length l_r computed from each individual k_b in the gyrokinetic simulation (blue curve) along with the average correlation length of the turbulence (green dashed line), both computed as the $1/e$ value of the corresponding CCF. The radial correlation length is largest for a finite $k_b\rho_s \approx 1.6$, and it becomes a decreasing function of k_b for larger wavenumbers. A power law $\sim C k_b^{-\alpha}$ is fitted to the l_r curve for larger wavenumbers ($k_b\rho_s \gtrsim 7$), giving an exponent $\alpha \approx 1.04$. This fit characterizes the scale-by-scale dependence of the radial correlation length corresponding to each binormal wavenumber k_b (or binormal wavelength). Together, figures 3(a) and (b) show that the average turbulent correlation length is different from the correlation length corresponding to each k_b. For the purpose of understanding radial correlation lengths measured via RCDR, this discussion shows that it is of crucial importance to take into account the scale by scale dependence of the radial correlation

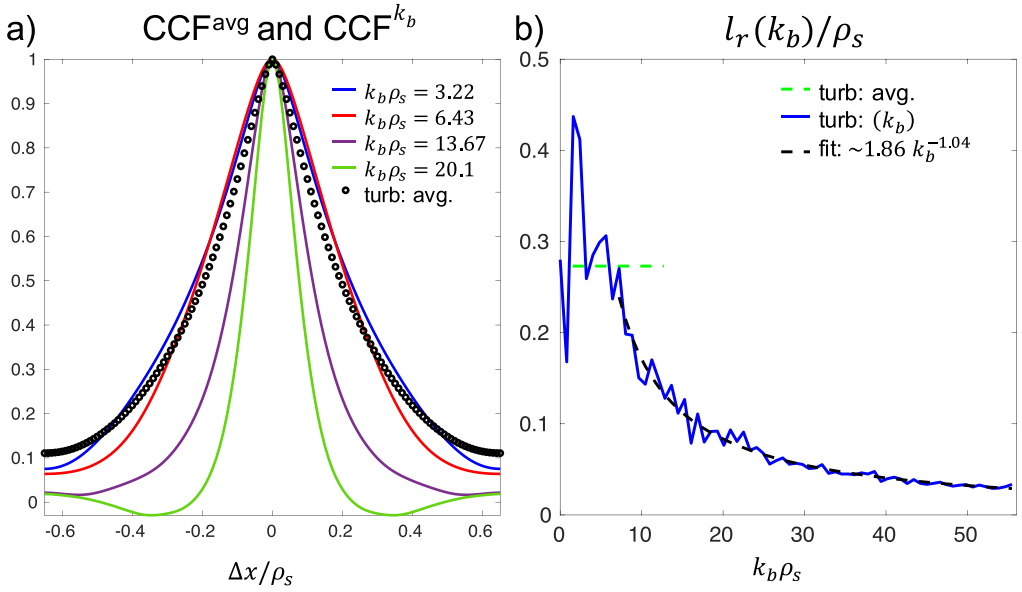

Figure 3. (a) Average turbulence cross-correlation function $\mathrm{CCF}^{\mathrm{avg}}$ (open black circles) and scale-dependent cross-correlation function for different k_b CCF^{k_b} in the electron-scale gyrokinetic simulation with $\gamma_E = 0$ (definitions in equation (4) and appendix B). (b) Scale-dependent radial correlation length $l_r(k_b)$ corresponding to each binormal wavenumber in the simulation (blue curve) along with the average correlation length of the turbulence (green dashed line). This curve describes the scale-by-scale dependence of l_r on k_b (no synthetic DBS is applied). The ion sound gyro-radius $\rho_s \approx 0.7$ cm is calculated with the local B and T_e.

length as only one wavenumber k_b is selected by a Doppler backscattering system.

The relationship $l_r \sim Ck_b^{-\alpha}$ with $\alpha \approx 1$ implies that the radial characteristic length l_r and binormal wavelength are proportional to each other scale-by-scale, that is, turbulent eddies in the power law fitting region (inertial range of the turbulent cascade) preserve their aspect ratio in x and y scale-by-scale. Larger k_b indicates smaller eddies in the binormal direction, which are also proportionally smaller in the radial direction. The constant of proportionality C can be interpreted as a rough measure of the eddy aspect ratio in the perpendicular (x, y) plane. We define a 'binormal correlation length' l_b as the $1/\mathrm{e}$ value of the sinusoidal oscillation corresponding to k_b, that is $l_b/\rho_s = \arccos(1/\mathrm{e})/k_b\rho_s \approx 1.19/k_b\rho_s$ (appendix B). A power law relationship of the form $l_r \sim Ck_b^{-\alpha}$ amounts to $l_r \sim C_r l_b^{\alpha}$ ($l_r/l_b \approx C_r = C\arccos(1/\mathrm{e})^{-\alpha}$). For $\alpha \approx 1$, the coefficient $C_r \approx l_r/l_b$ can be interpreted as the aspect ratio of the turbulent eddy between the radial and binormal directions. In this case, we find $C \approx 1.86$, yielding $l_r/l_b \approx 1.54 \approx 3/2$. This suggests that ETG-driven eddies *hypothetically* measured by DBS would exhibit an aspect ratio $l_r/l_b \approx 3/2$ in the (x, y) plane (at the outboard midplane of this specific NSTX condition). In RCDR experiments, a good approximation to the eddy aspect ratio is $l_r/l_b \approx l_r k_b/\arccos(1/\mathrm{e}) \approx l_r k_b/1.19$, where l_r and k_b can be easily obtained via the standard experimental analysis and tools.

The strong ETG drive of the present condition seems to contrast with the rather tight aspect ratio of $l_r/l_b \approx 3/2$. At first sight, this appears not entirely consistent with the radially elongated and poloidally thin ETG 'streamers' [83–85], and corresponds to lower aspect ratios than those inferred from ETG-driven turbulence in realistic gyrokinetic simulations of MAST $l_r/l_b \gtrsim 5$ [86, 87] and reported in NSTX $l_r/l_b \approx 4$ [88], as well as for the cyclone base case $l_r/l_b \approx 2$ [89] and early simulations for the W7-AS stellarator [90] $l_r/l_b \approx 2$. In fact, the eddy aspect ratio in real, physical space (x, y) can be strongly deformed when using the internally defined field-aligned coordinates of local flux tube simulations. The difference between the physical space (x, y) and the flux tube coordinates is accentuated in strongly shaped flux surfaces characteristic of the spherical tokamak. Using the GYRO internally-defined field-aligned coordinate system, one finds an aspect ratio ≈9 for the present condition, which would be characteristic of a radially elongated ETG 'streamer' (a factor of ×6 difference). However, we emphasize that internally-defined field-aligned coordinates do *not* yield a real aspect ratio in physical space, due to geometric effects such as flux-surface elongation, Shafranov's shift, etc. (details in table 1, appendix C). This realization further motivates the use of the normal and binormal (x, y) coordinates and the (k_n, k_b) wavenumber components for the purpose of quantitatively interpreting and projecting experimental measurements using gyrokinetic simulations.

Using the $l_r(k_b)$ relationship for calculating the aspect ratio of the turbulent eddies is accurate in the case where eddies are aligned with the radial direction x. For up-down symmetric flux-surface geometries, this can be the case at the outboard midplane $\theta = 0$ when the background $E \times B$ flow shearing rate γ_E is zero. It is well known that finite background $E \times B$ shear flow can stabilize (ion-scale) turbulence by tilting eddies in the perpendicular direction (x, y) and inducing radial decorrelation [91, 92]. Theoretically, a finite background $E \times B$ shear can break an underlying symmetry in the gyrokinetic equation, manifesting itself in an asymmetric

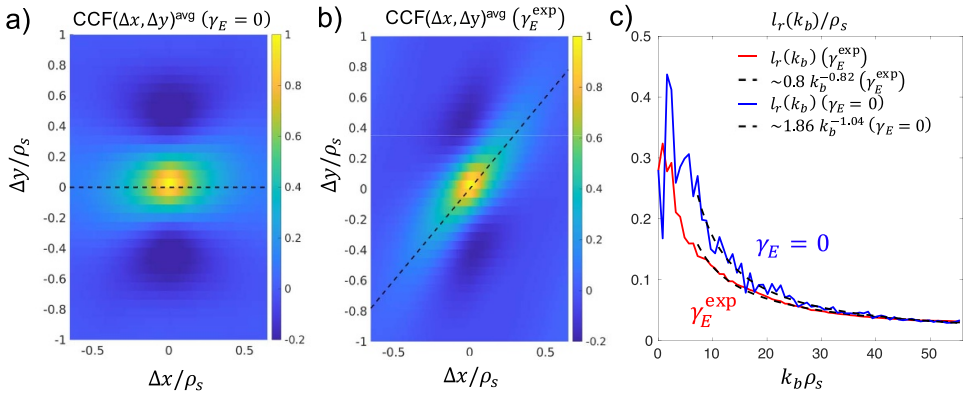

Figure 4. (a) 2D average turbulence correlation function corresponding to an ETG simulation with $\gamma_E = 0$ (figures 3). (x, y) are perpendicular to **B** and represent real lengths in the laboratory frame (they are not flux tube coordinates; details in appendices A and C). (b) 2D average turbulence correlation function for the same ETG simulation run with the experimental value of $\gamma_E \approx 0.13\ c_s/a$. Note the different tilt angle in (a) vs. (b). (c) Scale-dependent radial correlation length computed for each binormal wavenumber k_b corresponding to simulations in (a) and (b).

turbulent wavenumber spectrum [93] and yielding an eddy tilt. Accordingly, BES measurements in the core of DIII-D [94] have tilt angles $\theta_{\text{tilt}} \approx 10°$, while in the MAST core $\theta_{\text{tilt}} \gtrsim 45°$ have been reported [95, 96] in the presence of finite $E \times B$ shear. The effect of $E \times B$ flow shear on electron-scale turbulence is expected to be reduced due to the smaller correlation times. Even so, eddy tilt can be non-negligible in ETG-dominated regimes where ion-scale turbulence is suppressed by strong $E \times B$ flow shear, such as in low-to-modest β_e spherical tokamak scenarios. This has been suggested by nonlinear gyrokinetic simulations of ETG turbulence in the MAST and NSTX spherical tokamak core [87, 88]. An example of the ETG tilted eddies can be seen in figure 2.

In order to understand the effect of the background $E \times B$ shearing rate γ_E on the correlation length, an additional electron-scale simulation was performed, with identical input parameters and only differing by the finite, experimental value of the $E \times B$ shearing rate γ_E. Figure 4(a) shows the 2D correlation function $\text{CCF}_{2D}^{\text{avg}}$ in (x, y) computed from the density field δn corresponding to the $\gamma_E = 0$ case of figure 3. $\text{CCF}_{2D}^{\text{avg}}(\Delta x, \Delta y)$ is the generalization of the 1D CCF^{avg} from equation (4) (details in appendix B). As expected, the 2D correlation function exhibits no tilt in the (x, y) direction (noted by the black dashed line), showing that eddies tend to be aligned along x in the absence of $E \times B$ shear. The 1D radial cross-correlation function CCF^{avg} from figure 3(a) (black empty circles) can be read in figure 4(a) along the black dashed line $(\Delta y = 0)$. Note that the 2D $\text{CCF}_{2D}^{\text{avg}}$ becomes negative in the binormal y direction, which is indicative of the oscillatory nature of turbulence with finite k_{b}.

Figure 4(b) shows the 2D correlation function computed from the simulation using the experimental value of the $E \times B$ shearing rate $(\gamma_E \approx 0.13\ c_s/a)$. Notably, the 2D correlation function exhibits a finite tilt on the (x, y) plane, attributed to the finite γ_E. The eddy tilt can be further quantified by calculating the preferred direction of inclination on the (x, y) plane (details in appendix C). This yields a value of $\theta_{\text{tilt}} \approx 50°$ in the present ETG condition. As in the discussion of the eddy aspect ratio, this tilt angle value is the physical angle, in the real space laboratory frame, made by turbulent eddies at the outboard midplane, which is again enabled by the use of the (x, y) coordinates in this work. Using the GYRO field-aligned coordinate system at the outboard midplane would erroneously yield a tilt of $\theta_{\text{tilt}} \approx 11°$. This emphasizes once more the need to map field-aligned, flux tube coordinates to real, physical space to directly compare to experimental measurements. Previously reported eddy tilt angle values in the core of MAST using a BES diagnostic [95, 96] seem to be in agreement with the value of $\theta_{\text{tilt}} \approx 50°$ reported here.

The $l_r(k_b)$ curves corresponding to figures 4(a) and (b) are shown in figure 4(c). The blue curve corresponds to the $\gamma_E = 0$ case, which exhibits a larger correlation length than the finite γ_E case (red curve). A power law fit to the $l_r(k_b)$ curve with finite γ_E shows that $l_r \sim 0.8\ k_b^{-0.82}$, yielding an inferred eddy aspect ratio $C_r \approx 0.67$. As shown in appendix C, this value is different by a factor $\times 2$–3 with respect to the aspect ratio calculated along the tilted axes (black dashed lines in figures 4(a) and (b) and the corresponding perpendicular direction). The average aspect ratio of the turbulence in (x, y), computed as the ratio between the $1/\text{e}$ length-scales along the tilted axes increases by $\sim 20\%$ from $\gamma_E = 0$ to the finite γ_E case. The disagreement with the $l_r k_b$ estimate for finite γ_E (finite tilt) can be explained by the tilt of the eddies. A horizontal cut $(\Delta y = 0)$ of the $\text{CCF}_{2D}^{\text{avg}}(\Delta x, \Delta y)$ will yield a one dimensional correlation function that is affected by the oscillatory nature of the correlation function in the y-direction (with characteristic positive and negative values of the CCF). This decreases the value of the turbulence average correlation length l_r^{avg} as well as the scale-dependent correlation length $l_r(k_b)$, translating into a different value of the aspect ratio from the estimate given by $\approx l_r k_b / 1.19$.

The main lesson to retain from this discussion is that the eddy aspect ratio could be measured in RCDR experiments from the quantity $l_r k_b / \arccos(1/\text{e}) \approx l_r k_b / 1.19$ when the eddy tilt $\theta_{\text{tilt}} \approx 0$. For finite eddy tilt, $l_r k_b$ is not a good measure of the shape of the eddies, but it is related to their radial

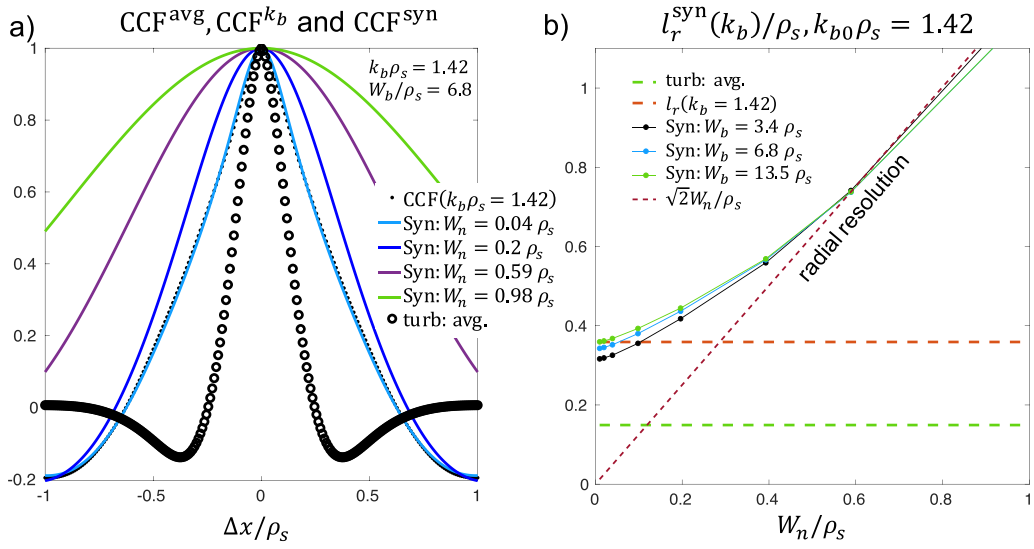

Figure 5. (a) Scale-dependent correlation function corresponding to electron-scale $k_b\rho_s = 1.42$ (CCF^{k_b}, black dots), synthetic correlation function for varying values of the radial resolution W_n ($\mathrm{CCF}^{\mathrm{syn}}$, colored curves), and average turbulence correlation function ($\mathrm{CCF}^{\mathrm{avg}}$, black circles). (b) Dependence of the synthetic radial correlation length computed as the $1/\mathrm{e}$ value from the synthetic radial correlation function $\mathrm{CCF}^{\mathrm{syn}}$, for different values of W_b ($W_b \gg 2\pi/k_b$). The radial correlation length from the selected wavenumber $k_b\rho_s = 1.42$ is only measurable when $l_r(k_b) \ll W_n$.

extent. In appendix C we provide additional details supporting and confirming these conclusions. A combination of the estimate proposed here to characterize the eddy aspect ratio ($l_r/l_b \sim l_r k_b/1.19$) and that proposed by Pinzón *et al* to measure the eddy tilt angle [97, 98] could be used in future studies to characterize the 2D eddy shape. Note that up-down asymmetric flux-surface geometries could introduce tilts in the (x, y) plane similar to those shown here, as well as off-midplane locations due to the effect of magnetic shear $\hat{s}$, but these are not the object of the present study.

3.2. *Influence of the diagnostic resolution* W_n

The previous section has highlighted the importance of taking into account the scale-by-scale variation of the radial correlation length of turbulent eddies for different wavenumbers k_b, encapsulated in the $l_r(k_b)$ relation in figure 3(b). Importantly, the analysis was independent of the synthetic DBS diagnostic, and was merely a discussion of the correlation properties of the turbulence. In this subsection, we turn to understanding how a DBS measurement can affect the interpretation of the measured radial correlation length.

We deploy the model DBS (equation (2)) to compute synthetic radial correlation lengths corresponding to the strongly driven ETG condition. We seek to understand the effect of the filter's radial dimension W_n, and fix the binormal dimension $W_b = 6.8\ \rho_s$ (the specific value is unimportant as long as $W_b \gg 2\pi/k_{b0}$ but is in accordance with existing DBS systems [37]). For this study, we use a simulation with a larger spatial domain $(L_r, L_\theta) \approx (20, 20)\rho_{s,\mathrm{unit}}$ to be able to scan realistic values of W_n. Figure 5(a) shows the cross-correlation functions $\mathrm{CCF}^{\mathrm{avg}}$, CCF^{k_b} and $\mathrm{CCF}^{\mathrm{syn}}$ computed using the formulas from equation (4), corresponding to the specific binormal wavenumber $k_b\rho_s = 1.42$ which exhibited the largest correlation length in the simulation. The empty, black circles show the average turbulence correlation function. The black dots show the scale-dependent correlation function CCF^{k_b} for $k_b\rho_s = 1.42$. The colored curves show the synthetic cross-correlation functions $\mathrm{CCF}^{\mathrm{syn}}$ computed for the same selected wavenumber, for varying values of the radial resolution $W_n = 0.04, 0.2, 0.59, 0.98\ \rho_s$ (and fixed binormal spot size $W_b = 6.8\ \rho_s$). Once more, the average turbulence correlation function is different from all the other correlation functions. In the case of small radial resolution ($W_n = 0.04\ \rho_s$), the synthetic correlation function converges to the scale-dependent correlation function CCF^{k_b} for $k_b\rho_s = 1.42$. This suggests that RCDR measurements are sensitive to the correlation function (and correlation length) of the specific, measured k_{b0} by DBS (routinely denoted $k_\perp$ in the literature), but not to the average turbulence correlation function $\mathrm{CCF}^{\mathrm{avg}}$ as previously discussed. This is relevant for interpreting correlation lengths measured via RCDR. Additionally, the synthetic correlation functions for increasing values of W_n are shown to become wider. Figure 5(b) shows the correlation lengths corresponding to the correlation functions in (a) as a function of W_n. Here, synthetic correlation lengths are also computed for different experimentally relevant values of the binormal spot size $W_b = 3.4, 6.8, 13.5\ \rho_s$. Importantly, figure 5(b) shows that the correlation length for large $W_b \gg 2\pi/k_{b0}$ and small W_n converges to the correlation length for $k_b\rho_s = 1.42$ (red dashed line). However, for increasing W_n, the synthetic correlation length is shown to asymptote linearly to the purple dashed line, which is the radial resolution W_n. This suggests that the diagnostic radial resolution W_n can itself strongly affect the value of the 'measured' correlation length in DBS experiments if the resolution is large enough, in agreement with previous work [33, 47]. The synthetic correlation length becomes dominated by the radial resolution when $W_n > l_r(k_{b0})$.

This discussion has emphasized the significant impact that the diagnostic resolution W_n can have on the measured DBS correlation length, where W_n has been artificially varied. The value of W_n remains an open question for Doppler backscattering. Previous work seems to suggest values in the order of the width of the Airy lobe W_{Ai} or the beam width, whichever is larger. It is well known that standard normal incidence reflectometry experiments are characterized by a radial spot size $W_{\mathrm{Ai}} \approx 0.5\, L_\epsilon^{1/3} \lambda^{2/3}$ [23, 30], corresponding to the width of the Airy lobe in the vicinity of the cutoff. Here L_ε is the permittivity scale length, equal to the density gradient scale length L_n in linear profile, slab geometry and O-mode polarization, while λ is the vacuum wavelength of the incident microwave beam. In the case of Doppler backscattering, it is possible that the Gaussian beam dimension near the cutoff might affect this reflectometry estimate W_{Ai}. The issue of the width of the beam near the reflection point is discussed analytically in [99, 100], which showed that the exact solution of the Helmholtz equation for linear profile, slab geometry and O-mode polarization exhibits a W_n at the cutoff location that becomes independent of the launching beam width for small incident launch angles, suggesting wave-effects can dominate, whereas beam width effects are more important for larger incidence angles. Ray tracing, beam tracing and full-wave simulations carried out in [101, 102] for realistic toroidal geometries of AUG seemed to agree with [99, 100], additionally suggesting that the Airy width W_{Ai} should be considered as a minimum value of W_n in experimental measurements.

Motivated by these works, we calculate the value of the width of the Airy lobe W_{Ai} for the present experimental condition in NSTX, yielding $W_{\mathrm{Ai}} \approx 2{-}4\ \rho_s$. This value is notably larger than the largest correlation length in this strongly-driven ETG simulation condition (recall $l_r(k_{b0}\rho_s = 1.4) \approx 0.4\ \rho_s$). Importantly, this suggests that radial correlation length measurements carried out for electron-scale $k_\perp$ DBS measurements are likely to be dominated by the radial resolution W_n, that is $l_r^{\mathrm{syn}} \to W_{\mathrm{Ai}}$, since the condition $W_n \gg l_r(k_{b0})$ is easily fulfilled.

These conclusions are reached using a highly simplified model for the DBS scattered amplitude (equations (2) and (3)), based on a Gaussian filter in the normal x and binormal y directions. However, the specific shape of the filter envelope function (Gaussian, Ai or other) should not affect the conclusion presented here, namely that measuring $l_r(k_{b0})$ using RCDR requires $W_n \ll l_r(k_{b0})$, and that condition is likely not satisfied for electron-scale DBS measurements. In other words, here we still expect the condition $W_n \gg l_r(k_{b0})$ to hold for non-Gaussian radial spot sizes, such as an Airy function. A resolution limit to the radial correlation measurement via RCDR was already observed in [33], and recent full-wave simulations using a Gaussian turbulence spectrum [47] have also shown that the synthetic radial correlation length can be increased by diagnostic effects. A more detailed explanation is given in appendix B. Having studied the radial correlation from an electron-scale turbulence simulation, the following section addresses whether W_n is also larger than $l_r(k_{b0})$ in conditions when a DBS reflectometer is sensitive to ion-scale wavenumbers.

4. Interpreting l_r from ion-scale turbulence

In this section we apply the previous analysis to a fully-developed, ion-scale ITG-driven turbulence regime in the mid-core of a JET NBI-heated ($P_{NBI} = 17$ MW) L-mode plasma, which is the object of recent momentum transport studies [71, 72]. Local, flux tube ion-scale nonlinear gyrokinetic simulations using the GS2 code [68] can simultaneously reproduce the ion thermal and momentum transport from the experimental estimates computed via TRANSP [80], while the electron heat flux was under-predicted but subdominant to the ion heat flux.

The gyrokinetic simulations were performed at $r/a \approx 0.5$, resolving two gyrokinetic species (e^-, D), including collisions ($\nu_{ee} \approx 0.02\ a/v_{tr}, \nu_{ii} \approx 0.00026\ a/v_{tr}$), background flow and flow shear ($M \approx -0.08, \gamma_E \approx -0.05\ a/v_{tr}, \gamma_p \approx 0.2\ a/v_{tr}$) and electrostatic fluctuations. The r subscript in v_{tr} refers to the reference species values, which was chosen to be deuterium in these simulations. Periodic boundary conditions were employed in the perpendicular dimensions x and y, while the twist-and-shift boundary condition [103, 104] was employed using a newly developed wavenumber-shifting method [71, 72]. A typical simulation domain for ion-scale turbulence was employed, with radial and poloidal box sizes on the order of $(L_\mathrm{x}, L_\mathrm{y}) \approx (77, 70)\rho_r$, equating to radial and poloidal wavenumber resolutions $k_\mathrm{x}\rho_r \in [0.08, 4.79]$, $k_\mathrm{y}\rho_r \in [0.09, 2.07]$. Here k_x and k_y are the radial and poloidal wavenumbers internally defined in GS2, which are related to k_n and k_b as shown in appendix A, and ρ_r is the GS2 internally defined gyroradius (appendix A).

Parallel resolution employed 33 poloidal grid points in a 2π domain, 16 energies and 37 pitch-angles (20 passing, 17 trapped). This choice of numerical grids was made according to convergence and accuracy tests performed for the present condition [71, 72]. The flux surface geometry is described by a Miller equilibrium [82].

4.1. Scale-dependent, physical correlation length

In the case of ITG-driven, ion-scale turbulent fluctuations ($k_\perp \rho_s \lesssim 1$), one naturally expects larger radial correlation lengths than for electron-scale turbulence. This begs the question whether the condition $l_r(k_{b0}) > W_n$ could be satisfied in these conditions.

Similar features to the electron-scale turbulence can be observed in these ion-scale turbulence simulations. We consider the more realistic $\gamma_E = \gamma_E^{\mathrm{exp}}$ case first. Figure 6(a) shows the average turbulence correlation function $\mathrm{CCF}^{\mathrm{avg}}$ (black, empty circles) vs. the correlation function for a subset of binormal wavenumbers $k_b\rho_s = 0.15, 0.34, 0.64, 1.13$ (colored curves) corresponding to this ITG-driven turbulence condition. The average turbulence correlation function differs from the scale-dependent correlation function of each k_b, which becomes narrower for larger k_b, similar to what was observed analyzing electron-scale turbulence in figure 3(a). The $1/\mathrm{e}$ correlation length for each k_b is plotted in figure 6(b), showing a peak correlation length for $k_b\rho_s \approx 0.14$, and a decrease for larger k_b. Fitting a power law to the correlation length for $k_b\rho_s \gtrsim$

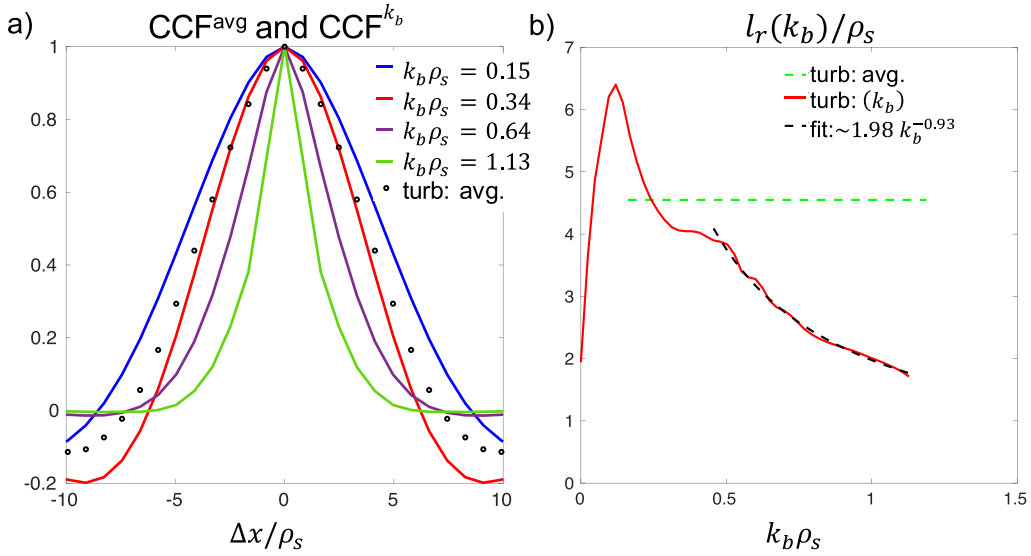

Figure 6. Similar to figure 3 for ion-scale turbulence with $\gamma_E = \gamma_E^{\rm exp}$. (a) Average turbulence cross-correlation function $\mathrm{CCF}^{\rm avg}$ (open black circles) and cross-correlation function for different k_b CCF^{k_b} in the ion-scale gyrokinetic simulation. (b) Radial correlation length l_r corresponding to each binormal wavenumber in the simulation. Note that the radial correlation length corresponding to ion-scale k_b (ITG-driven turbulence) exhibits a very similar dependence with k_b as ETG-driven turbulence (figure 3). In this condition, $\rho_s \approx 0.33$ cm.

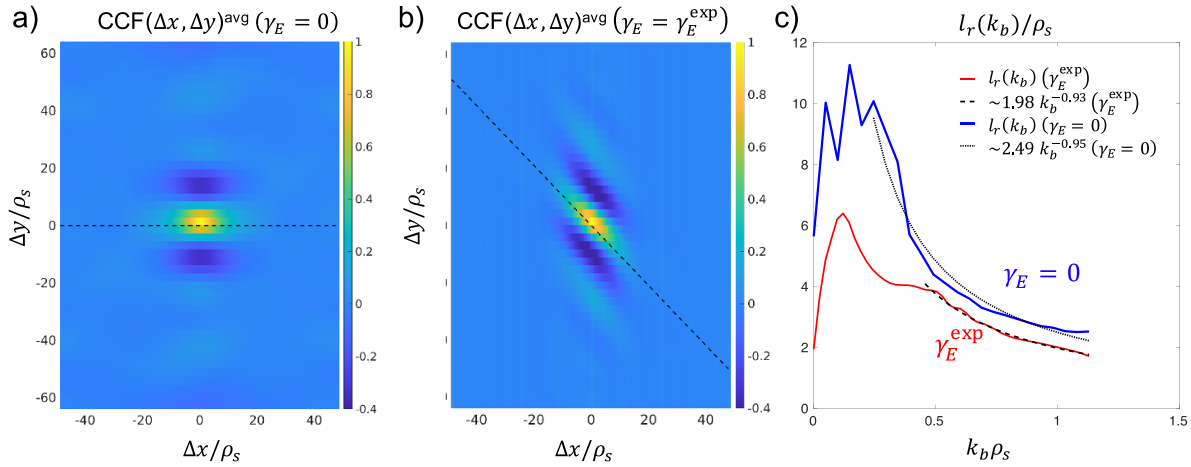

Figure 7. Similar to figure 4 for ion-scale turbulence simulation in JET. (a) 2D average turbulence correlation length run with value of $\gamma_E = 0$. (b) 2D average turbulence correlation length run with the experimental value of γ_E. (c) Radial correlation length computed for each binormal wavenumber k_b corresponding to simulations in (*a*) and (*b*).

0.5 yields $l_r \sim 1.98\ k_b^{-0.93}$. Inferring an eddy aspect ratio from such a measurement would yield $C_r \approx 1.68$, although we now know that the $l_r k_{b0}$ estimate is not the same as the one found using tilted axes in the finite γ_E, finite $\theta_{\rm tilt}$ case. A more detailed analysis of the 2D correlation function yields an aspect ratio of $l_r/l_b \approx 3.1$ along the tilted axes (appendix C). The scale-dependent correlation length in figure 6(b) exhibits a 'plateau' for $k_b\rho_s \approx 0.3$–0.5. This could be a physical signature of the specific turbulent state, or it could be an artefact of the eddy tilt induced by the background $E \times B$ shear. For this reason, we chose to fit the function for $k_b\rho_s \gtrsim 0.5$.

As in the electron-scale case, an additional nonlinear gyrokinetic simulation was performed with GS2, only differing from the first one by the zero $E \times B$ shearing rate value ($\gamma_E = 0$). The 2D correlation functions in the (x, y) plane for both conditions are shown in figures 7(a) and (b), showing once more the tilting induced by the background $E \times B$ shear on the turbulence, while the simulation with zero γ_E exhibits no appreciable tilt. Figure 7(c) shows the corresponding radial correlation length $l_r(k_b)$ from each binormal wavenumber k_b in each simulation. The simulation without $E \times B$ shear (blue) exhibits a larger correlation length. The power law fit $l_r \sim 2.49\ k_b^{-0.95}$ suggests an eddy aspect ratio $l_r/l_b \approx 2.11$ when $\gamma_E = 0$. This aspect ratio is consistent with the average turbulence aspect ratio computed from the 2D correlation function, which yields $l_r/l_b \approx 1.88$ in this $\gamma_E = 0$ case (appendix C). This value is in a similar range to previously measured eddy aspect ratios of ion-scale turbulent fluctuations using BES, showing $l_r/l_b \approx 2$–3 in conventional tokamaks such as DIII-D [94, 105] and TFTR [10]. Interestingly, BES measurements in

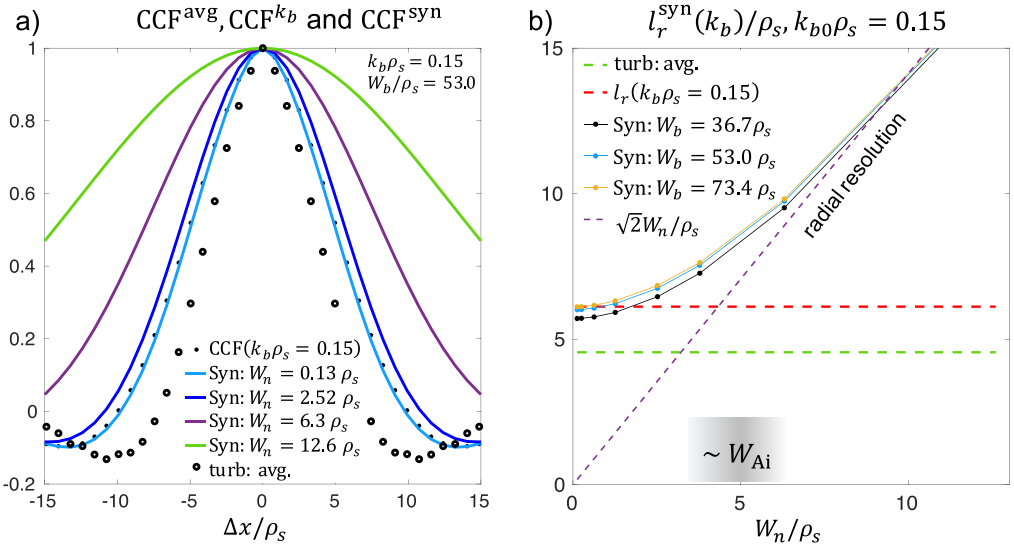

Figure 8. Similar to figure 5 for ion-scale turbulence simulation in the JET core. (a) Scale-dependent correlation function corresponding to electron-scale $k_b\rho_s = 0.15$ (CCF^{k_b}, black dots), synthetic correlation function for varying values of the radial resolution W_n ($\mathrm{CCF}^{\mathrm{syn}}$, colored curves), and average turbulence correlation function ($\mathrm{CCF}^{\mathrm{avg}}$, black circles). (b) Dependence of the synthetic radial correlation length computed as the $1/\mathrm{e}$ value from the synthetic radial correlation function $\mathrm{CCF}^{\mathrm{syn}}$, for different values of W_b ($W_b \gg 2\pi/k_b$). The condition $l_r(k_b) \gtrsim W_n$ is more easily satisfied for ion scales than for electron scales, but suggests that the diagnostic radial resolution still likely affects l_r^{syn}. The estimated width of the first Airy lobe W_{Ai} is indicated for reference.

the MAST spherical tokamak [95, 96, 106, 107] have yielded inverted aspect ratios $l_r/l_b \approx 1/4{-}1/2$, which could be related to the suppression of ion-scale turbulence in MAST, and are also likely affected by the strongly shaped nature of spherical tokamak flux surfaces (inducing radial compression and poloidal elongation at the outboard midplane). As in the previous section, the quoted aspect ratio $l_r/l_b \approx 1.88$ corresponds to the real, physical aspect ratio perpendicular to **B**. Using the internal, field-aligned coordinates in GS2 for the present case would have yielded a value $l_r/l_b \approx 2.99$, a $\sim$60% difference with respect to the physical aspect ratio (for $\gamma_E = 0$). The difference is lower than the factor of $\times 6$ error in the previous NSTX case due to the lower flux-surface shaping in this JET L-mode case. However, this suggests that quantitative comparisons of the eddy aspect ratio between experiments and simulation of conventional tokamaks require carefully considering physical (x, y) coordinates (or equivalent), and not the internally defined field-aligned coordinates characteristic of gyrokinetic codes.

It is worth noting that the radial correlation length (along the physical x-direction) is reduced by the effect of flow shear (figures 4(c) and 7(c)). Conversely, the eddy aspect ratio l_r/l_b along the tilted axes is enhanced by the effect of flow shear: $l_r/l_b \approx 1.88$ for $\gamma_E = 0$, while $l_r/l_b \approx 3.1$ for γ_E^{exp}. This is consistent with the induced eddy tilt and the effect of the binormal structure of the turbulence: the oscillatory nature of the correlation function in the y-direction has the effect of reducing the effective correlation length along the physical x-direction (figures 4(c) and 7(c)), even when the aspect ratio along the tilted axes increases for finite γ_E. This effect is qualitatively observable in figures 7(a) and (b), as well as for the electron-scale case in figures 4(a) and (b) from section 3, where the aspect ratio along the tilted axes takes the values $l_r/l_b \approx 1.54$ for $\gamma_E = 0$, while $l_r/l_b \approx 1.98$ for γ_E^{exp}.

Analysis shows that the eddy tilt for the experimental value of $E \times B$ shear in this JET mid-core plasma is $\theta_{\mathrm{tilt}} \approx -(40°{-}45°)$. In the previous section we saw that the eddy tilt in physical space can be strongly affected by the strong shaping characteristic of a spherical tokamak (by a factor $\times 5$–6 in the previous NSTX condition), which is not the case for the present JET condition. The tilt is also affected by the characteristic length and timescales of the particular eddy under consideration, which differs between electron and ion scale turbulence.

4.2. *Influence of the diagnostic resolution* W_n

In the case of ion-scale turbulence, the effect of finite diagnostic radial resolution W_n is similar to electron-scale turbulence, meaning $l_r^{\mathrm{syn}} \to W_n$ for $W_n \gg l_r(k_{b0})$. However, given ion-scale fluctuations exhibit larger correlation lengths, the condition $W_n < l_r(k_{b0})$ for a realistic $W_n \sim W_{\mathrm{Ai}}$ is now more easily satisfied. Figure 8(a) shows the average turbulence correlation function (black circles), the scale-dependent correlation function for $k_b\rho_s = 0.15$ (black dots), which exhibits the largest correlation length in the simulation, and the synthetic correlation function for varying values of the radial resolution W_n, at fixed binormal spot size $W_b = 53.0\ \rho_s$. As in figure 5(a), the synthetic correlation function for small $W_n = 0.13\ \rho_s$ converges to the scale-dependent correlation function for $k_b\rho_s = 0.15$, while for higher W_n, the synthetic correlation function gets wider and wider. Figure 8(b) shows the variation of the $1/\mathrm{e}$ synthetic correlation length with W_n. Once again, the correlation length converges to the correlation length of $k_{b0}\rho_s =$

0.15 for all values of W_b when $W_n \ll l_r(k_{b0})$ ($W_b \gg 2\pi/k_b$), and it asymptotes to the radial resolution W_n for $W_n \gg l_r(k_{b0})$. Note, however, that now the condition $W_n \approx l_r(k_{b0})$ occurs for a larger correlation length $l_r(k_{b0}\rho_s = 0.15) \approx 5\ \rho_s$. Evaluating the reflectometry estimate for the radial spot size $W_n \sim W_{\rm Ai} \approx 0.5\ L_n^{2/3}\lambda^{1/3}$ for the current conditions gives $W_{\rm Ai} \approx 4$–$6\ \rho_s$. This suggests that experimentally relevant W_n are likely to affect a measured RCDR correlation length, but in a less dramatic way than for electron-scale fluctuations. The effect is not completely negligible, as demonstrated by figure 8(b).

5. Discussion of the use of separable turbulence spectra

In the previous sections, we have used a simple model DBS (equations (2) and (3)) and realistic turbulence spectra from nonlinear gyrokinetic simulations to understand the turbulence properties and the diagnostic effects relevant to RCDR measurements. Realistic turbulence spectra naturally yield a relationship $l_r(k_b) \sim Ck_b^{-\alpha}$, illustrated in figures 3 and 6. In this section, we discuss the consequences of modelling RCDR using turbulence spectra that are unable to capture the dependence of the radial correlation length on the binormal scale. Such flawed spectra has become a common practice in the community [33, 41, 42, 47, 60–62, 97, 98].

The dependence of the radial correlation length on the binormal scale is encoded in the ensemble averaged turbulent wavenumber spectrum of the density fluctuations $\langle|\delta\hat{n}(k_n,k_b)|^2\rangle_T$. Importantly, previous theoretical and numerical studies [41, 62] (as well as many other works [33, 42, 47, 60, 97, 98]) used a separable turbulence wavenumber spectrum in the k_n and k_b components, written as a product of two independent functions h_n and h_b, $\langle|\delta\hat{n}(k_n,k_b)|^2\rangle_T = h_n(k_n)h_b(k_b)$. This results in $l_r(k_b) = l_r^{\rm avg}$, which does not accurately represent magnetized plasma turbulence in the tokamak core. To understand the consequences of using a separable turbulence spectrum in k_n and k_b, we use the characteristic expansion of the density fluctuation field $\delta n(x,y,\theta,t) = \sum_{k_n,k_b}\delta\hat{n}(k_n,k_b,\theta,t)e^{ik_nx+k_by}$ as treated in a local flux tube (equation (1), applicable to GYRO and GS2 in particular). We substitute this expression for δn into the expression for the model scattered amplitude A_s from equation (2), and use that to compute the synthetic CCF$^{\rm syn}$ from equation (4), yielding equation (5):

$$\mathrm{CCF}^{\rm syn}(\Delta x) = \frac{\sum_{k_n,k_b} e^{-k_n^2W_n^2/2}e^{-(k_b-k_{b0})^2W_b^2/2}\langle|\delta\hat{n}(k_n,k_b)|^2\rangle_T e^{ik_n\Delta x}}{\sum_{k_n,k_b} e^{-k_n^2W_n^2/2}e^{-(k_b-k_{b0})^2W_b^2/2}\langle|\delta\hat{n}(k_n,k_b)|^2\rangle_T}, \quad (5)$$

which is valid for general W_n and W_b. Next we set the experimentally relevant value of $W_b \gg 2\pi/k_{b0}$, we place ourselves in the best possible scenario where $W_n \ll l_r(k_{b0})$, and we neglect the effect of the varying k_{b0} between the different DBS diagnostic channels. This yields:

$$\mathrm{CCF}^{\rm syn}(\Delta x) \to \frac{\sum_{k_n}\langle|\delta\hat{n}(k_n,k_{b0})|^2\rangle_T e^{ik_n\Delta x}}{\sum_{k_n}\langle|\delta\hat{n}(k_n,k_{b0})|^2\rangle_T} \equiv \mathrm{CCF}^{k_{b0}}(\Delta x)$$

for

$$W_b \gg 2\pi/k_{b0}$$

and

$$W_n \ll l_r(k_{b0}). \quad (6)$$

Equation (6) analytically shows that the synthetic radial correlation function CCF$^{\rm syn}$ will be a good representation of the scale-dependent CCF^{k_b} under these assumptions. This was already observed in the previous sections, particularly in figures 5 and 8. Importantly, this correlation function CCF$^{\rm syn}$ depends on the measured k_b via the turbulence spectrum, which is not in general separable into its k_n and k_b coordinates (we have omitted the $\theta = 0$ and time t variables for clarity in equation (6)). Expression (6) contains the dependence of l_r with k_b encoded through the turbulence spectrum. Using a separable turbulence spectrum $\langle|\delta\hat{n}(k_n,k_b)|^2\rangle_T = h_n(k_n)h_b(k_b)$ (Gaussian, Lorentzian, top-hat, etc.) will yield a radial correlation length l_r that becomes independent of k_b (substitute $h_n(k_n)h_b(k_b)$ into equation (6)). This means that a separable turbulence spectrum of the form $\langle|\delta\hat{n}(k_n,k_b)|^2\rangle_T = h_n(k_n)h_b(k_b)$ cannot contain the scale-by-scale variation of realistic turbulence spectra, which can have important implications for interpreting and projecting RCDR measurements. The average correlation length $l_r^{\rm avg}$ (computed from CCF$^{\rm avg}$) and the scale-dependent correlation length $l_r(k_b)$ become identical for separable wavenumber spectra.

A proposed analytical expression for nonseparable, density fluctuation wavenumber power spectra inspired by the power law spectra characteristic of gyrokinetic simulations, and which contains the scale-by-scale dependence of the radial correlation length, is:

$$\left\langle\left|\frac{\delta\hat{n}}{n}(k_n,k_b)\right|^2\right\rangle_T = \frac{D}{1+\left(\frac{|k_n|}{w_{k_n}}\right)^{\gamma}+\left(\frac{|k_b-k_{b*}|}{w_{k_b}}\right)^{\beta}}. \quad (7)$$

In this expression, the spectral exponents γ in k_n and β in k_b are allowed to differ. w_{k_n} and w_{k_b} represent the spectral widths of the turbulence wavenumber spectrum, and are related to the average turbulence radial and binormal correlation lengths by $w_{k_n} \propto 1/l_r$ and $w_{k_b} \propto 1/l_b$. The spectrum in k_b is allowed to peak at a finite $k_b = k_{b*}$, consistent with the linear drive for typical micro-instabilities in the tokamak core peaking at finite values of k_b, and representing the injection driving scale of the turbulence (typically $k_{b*}\rho_s \approx 0.1$–0.6 for ITG, $k_{b*}\rho_s \approx 2$–30 for ETG, etc.). The spectrum from equation (7) is chosen to represent spectra in the absence of tilt angle $\theta_{\rm tilt}$ ($\gamma_E = 0$ and up-down symmetric flux surfaces at the outboard midplane $\theta = 0$). This results in a symmetric spectrum in k_n, which is enforced by the absolute value $|k_n|$. Representing the effect of flow shear or nonsymmetric spectra with a finite tilt angle could easily be obtained via a rotation of the $\mathbf{k}_\perp = (k_n,k_b)$ perpendicular wave-vector, which would result in a finite peak at normal wavenumber k_{n*}.

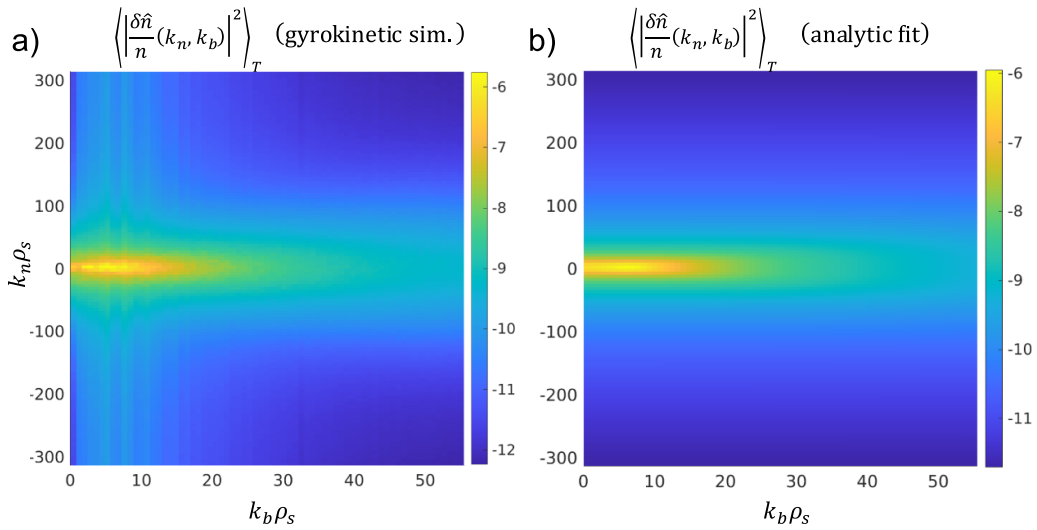

Figure 9. (a) Time-averaged density fluctuation power spectrum $\langle|\delta\hat{n}/n(k_n,k_b)|^2\rangle_T$ from electron-scale nonlinear gyrokinetic simulation in section 3 ($\gamma_E = 0$). (b) Bidiminensional fit in (k_n,k_b) to the simulated $\langle|\delta\hat{n}/n(k_n,k_b)|^2\rangle_T$ using the analytical spectral shape from equation (7).

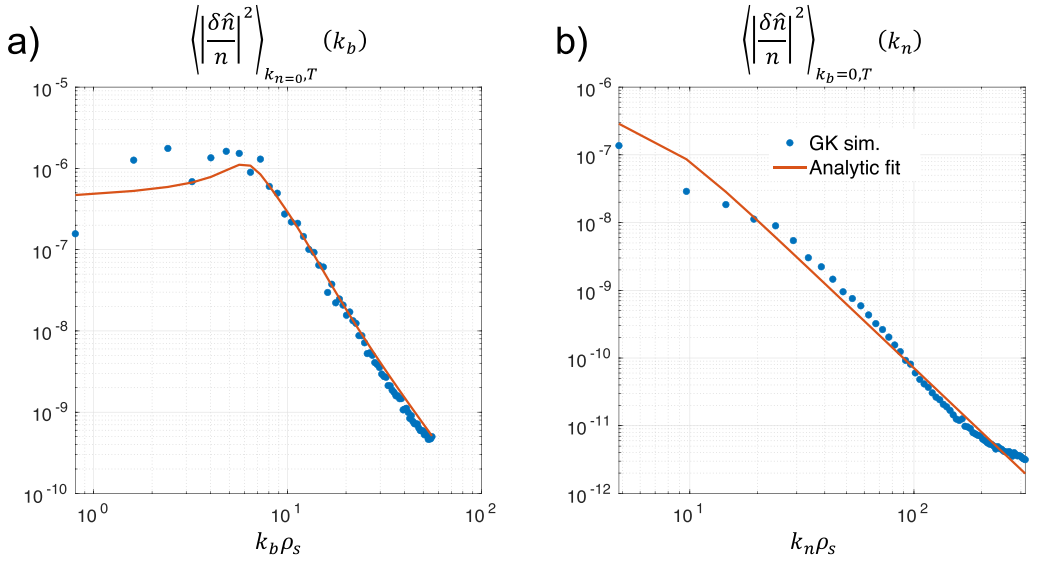

Figure 10. (a) Comparison between the time-averaged, gyrokinetic density fluctuation power spectrum (blue dots) and the analytic fit to the simulation spectrum using formula (7), plotted against binormal wavenumber $k_b\rho_s$. (b) Gyrokinetic spectrum and analytic fit with respect to normal wavenumber $k_n\rho_s$. Both correspond to the electron-scale, ETG-driven condition in section 3.

In order to illustrate the characteristics of the proposed analytic spectrum, the spectral shape from equation (7) is fit to the time-averaged spectrum computed from nonlinear gyrokinetic simulation corresponding to the strongly-driven ETG condition of section 3. The 2D spectrum in (k_n,k_b) from gyrokinetic simulation is compared with the analytical fit in figures 9(a) and (b). The analytical fit is shown to qualitatively represent the dominant spectral features of the 2D spectrum in (k_n,k_b). In order to quantitatively assess the fit, the simulated spectrum is compared to the analytical fit separately in the k_n and k_b directions in figures 10(a) and (b). The spectral dependence with k_b (for $k_n = 0$) is shown to satisfactorily reproduce the main characteristics of the gyrokinetic spectrum, capturing a peak wavenumber $k_b\rho_s \approx 5{-}7$, and also the expected power law dependence of larger wavenumbers $k_b\rho_s \gtrsim 10$. The spectral dependence in k_n ($k_b = 0$) is monotonously decreasing, and the analytic expression is once more shown to recover the power law dependence in this dimension. The fitted analytical expression (7) for this specific strongly driven ETG simulation yields the following fit parameters: $\gamma \approx 2.88, \beta \approx 3.14, w_{k_n}\rho_s \approx 3.71, w_{k_b}\rho_s \approx 4.97, k_{b*}\rho_s \approx 5.60, D \approx 6.3\ 10^{-3}\ (\rho_s/a)^2$.

To test how well the proposed spectral shape represents the dependence of the radial correlation length with k_b, we compute the scale-dependent correlation function CCF^{k_b} directly from the spectrum (equations (6) and (16) in appendix B), and then compute the scale-dependent correlation length $l_r(k_b)$ as in the rest of the manuscript. The analytic expression of the

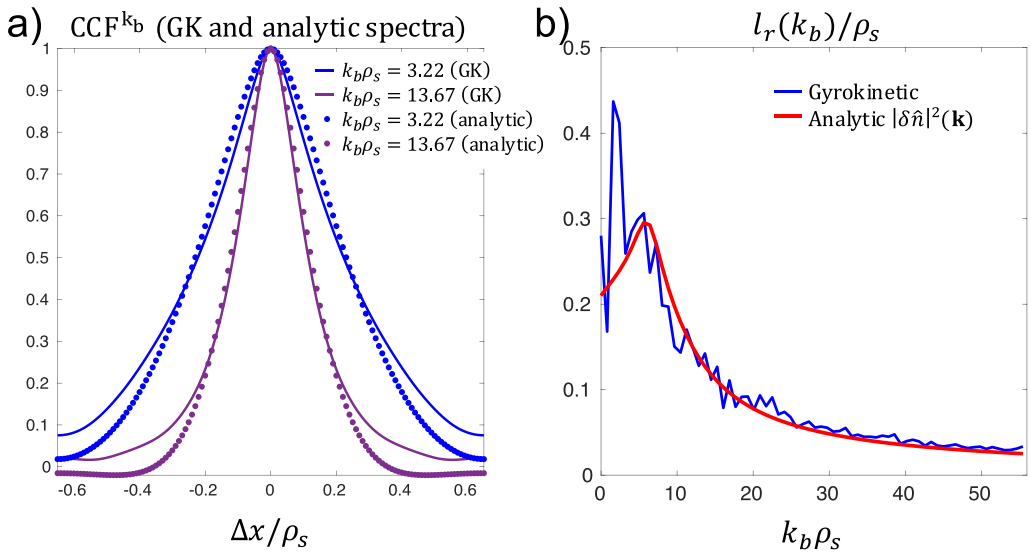

Figure 11. (a) Scale-dependent correlation function CCF^{k_b} directly computed from gyrokinetic simulation (thick lines) from two wavenumbers $k_b\rho_s = 3.22, 13.67$, compared to the scale-dependent correlation function computed using the analytic fit to the wavenumber spectrum from equation (7) (colored dots). (b) Scale-dependent correlation length for all wavenumbers k_b in the simulation, using gyrokinetic spectrum (blue) and analytic fit from equation (8) (red).

spectrum gives an analytic expression for $l_r(k_b)$, which has the following functional dependence:

$$l_r(k_b) \sim \frac{\text{const.}}{w_{k_n}} \frac{1}{\left[1 + \left(\frac{|k_b - k_{b*}|}{w_{k_b}}\right)^{\beta}\right]^{1/\gamma}}. \tag{8}$$

Similarly to the spectrum in equation (7), the analytic expression for $l_r(k_b)$ exhibits a peak correlation length at $k_b \approx k_{b*}$. The correlation length is shown to be inversely proportional to the spectral width w_{k_n}, which follows from the Fourier transform relationship between $\langle|\delta\hat{n}(k_n, k_b)|^2\rangle_T$ and $\mathrm{CCF}^{k_b}(\Delta x)$ (equation (6)). Equation (8) also exhibits the power law dependence $l_r \sim k_b^{-\beta/\gamma}$ for large k_b. Recalling that the turbulent eddies have a scale-invariant aspect-ratio when $l_r \sim k_b^{-1}$, this shows that the density fluctuation wavenumber power spectrum in equation (7) will result in scale-invariant eddy aspect-ratios when $\gamma = \beta$. In this specific condition, we find $\beta/\gamma \approx 1.1$, which is reasonably close to 1. The eddy aspect ratio here can be calculated as $l_r/l_b \propto w_{k_b}/w_{k_n} \approx 1.34$, which is reasonably close to the value $l_r/l_b \approx 1.54$ reported for this same condition in section 3. In figure 11(a) we compare the scale-dependent correlation function CCF^{k_b} of the gyrokinetic (thick lines) and analytic spectra fit (colored dots), corresponding to two different wavenumbers $k_b\rho_s = 3.22, 13.67$. The scale-dependent correlation functions are shown to be satisfactorily reproduced by the analytic expression for the spectrum. The scale-dependent correlation length $l_r(k_b)$ computed for all k_b is also shown to be well reproduced by the analytic spectrum in equation (7), as shown in figure 11(b). This discussion motivates a preferential use of realistic spectra, gyrokinetic or analytic expressions as in equation (7), above the use of separable spectra (Gaussian, Lorentzian, top-hat, etc.) in future modelling works of RCDR. For reference, similar analysis carried out for the ion-scale ITG-driven turbulence condition in section 4 gives the following fit parameters: $\gamma \approx 3.90, \beta \approx 3.24, w_{k_n}\rho_s \approx 0.17, w_{k_b}\rho_s \approx 0.28, k_{b*}\rho_s \approx 0.24, D \approx 0.0395\ (\rho_s/a)^2$. In this condition, we find the exponent $\beta/\gamma \approx 0.83$, while $l_r/l_b \approx w_{k_b}/w_{k_n} \approx 1.65$, which is consistent with the aspect ratio calculated from the 2D correlation function $l_r/l_b \approx 1.88$ in section 4. These parameters might be more relevant to predominantly ion-scale driven turbulent fluctuations (ITG/TEM) in the core of conventional tokamak scenarios, while the previous ETG case might be more relevant to predominantly ETG-driven and suppressed ion-scale turbulence, as in some plasma scenarios in the core of spherical tokamaks.

It is interesting to contrast the relationship $l_r \sim C\, k_b^{-\alpha}$ with other works, from experiments to modelling and theory. In this work, this is a mere consequence of the scale-by-scale dependence of the radial and binormal length scales of the turbulence, which is itself a consequence of the non-separable, power law character of the turbulent spectrum (equation (7)). The first RCDR radial correlation length measurements were performed by Schirmer *et al* for an ASDEX-U discharge in [33]. These pioneering measurements, coupled to full-wave simulations argued that the measured radial correlation length is independent of the measured $k_\perp$ (although only a restricted range of $k_\perp$ was analyzed). The same dependence is also observed in the nonlinear response regime [108] as shown by full-wave simulations [62] and experimental measurements [109], but was not the object of the present work. Analytical theory by Gusakov *et al* [41, 61] and full-wave simulations by Blanco *et al* [62] suggested that the radial correlation length is a monotonically decreasing function of the antenna tilt angle when operating in the linear response regime. This is a similar observation to what we find. The incident angle

of the launching microwave antenna with respect to the horizontal is directly related to the measured k_b at the cutoff location ($k_b = 2\ k_i \sin\theta_i$ in slab geometry, where k_i is the microwave wavenumber and θ_i the vertical incident antenna angle). In [41, 61, 62] it was argued that the poorly localized forward scattering contribution is suppressed once the antenna tilt angle surpasses a critical launch angle, which should result in correlation length measurements by RCDR similar to the true radial correlation length. Experiments by Fernández-Marina *et al* [109] performed at the TJ-II stellarator seemed to confirm the theoretical and full-wave simulation results [41, 42, 61, 62] in the linear response regime. Importantly, these works used a separable turbulence wavenumber spectrum in the k_n and k_b components (top-hat, Gaussian or Lorentzian in shape), which do not contain the scale-by-scale dependence characteristic of the turbulence, and result in $l_r(k_b) = l_r^{\text{avg}}$, which does not accurately represent magnetized plasma turbulence in the tokamak core. Therefore, the proposed explanation for the observed inverse proportionality of l_r^{exp} with the incidence angle was the poorly localized forward scattering contribution of the microwave beam along the path, which can increase the measured radial correlation length at small antenna incidence angles, that is small k_b. This effect disappears for large enough antenna incidence angles (large k_b), therefore yielding an inverse proportionality relationship between l_r and k_b. With our results, we suggest another possible explanation. The observed inverse dependence of l_r^{exp} on k_b could be a characteristic of the turbulence.

The proposed relationship $l_r(k_b) \sim k_b^{-\alpha}$ appears to be a universal, robust characteristic of the turbulence, as shown by nonlinear gyrokinetic simulation of ETG and ITG-driven turbulence in sections 3 and 4 and many other similar simulations. This may explain, or contribute to the explanation of, the observed decrease of the measured radial correlation length with the k_b selected by DBS [109] (denoted $k_\perp$ in the literature). The fact that analytical work [41, 61] and full-wave simulations [62] show that separable spectra (Gaussian, top-hat, Lorentzian, etc.) yield a measured l_r dependent on k_b suggests that a combination of two effects, the scale-by-scale variation of l_r with $k_\perp$ and a diagnostic effect (forward scattering) may explain the experimental observations [109]. For this reason, an analytic, realistic power law spectrum (equation (7)) is proposed in this section, which could be used in future works to model the DBS response using full-wave or analytical calculations.

6. Conclusions and discussion

In the present manuscript we have highlighted several important considerations to be taken into account when performing radial correlation measurements via the RCDR technique. The conclusions are reached by using a simplified model DBS for the scattering amplitude and deploying it on two specific tokamak core conditions: a highly unstable ETG regime in the outer core of an NSTX moderate-β_e plasma, and a fully developed ITG turbulence regime in the mid core of a JET L-mode plasma.

The two conditions are chosen as representative of electron and ion-scale turbulent fluctuations for potential RCDR measurements. The measured $k_\perp \rho_s$ from different DBS systems around the world [33, 37, 40, 43–46, 49–59, 109] (illustrated in figure 1) are shown to exhibit a close correlation with the local value of electron beta β_e. The correlation is shown to agree with a simple scaling $k_\perp \rho_s \sim (m_i/m_e)^{\frac{1}{2}} \beta_e^{\frac{1}{2}}$, which can be explained by assuming O-mode polarization of the incoming microwaves and ignoring the important effect of the incident antenna tilt angle in the measured $k_\perp$. However, when scanning approximately four orders of magnitude in β_e, in very different plasma conditions (and different antenna incidence angles), the 'analytic' scaling seems to agree fairly well with the DBS measurements as shown in figure 1. This highlights that DBS can be sensitive to ion- and electron-scale density fluctuations: the former will likely take place in low-β_e conditions (low performance plasmas, at the pedestal or in high-field devices), while the latter will preferentially take place for larger β_e values (high performance plasmas, at the deep core or in spherical tokamaks). Perhaps the clearest example of this comes from the JET data points, where the low-β_e cases correspond to edge measurements in low performance plasmas [57, 58], while the high-β_e cases correspond to deep core measurements in high β_N discharges. This scaling is *not* intended to be accurate for predicting the measured $k_\perp \rho_s$ in specific experiments, and is *not* intended to be an equality between $k_\perp \rho_s$ and β_e, but merely seeks to illustrate how the measured $k_\perp \rho_s$ can be affected by large variations in β_e.

This work has also highlighted that RCDR measurements are not sensitive to the average correlation length of the turbulence, but are sensitive to the scale-dependent correlation length $l_r(k_{b0})$ corresponding to the measured k_{b0} (in conditions where $l_r(k_{b0}) \gg W_n$). Notably, this is a different quantity from the radial correlation length measured by other core fluctuation diagnostics such as BES [10, 11], PCI [14–16], CECE [18, 19] and conventional reflectometry [22, 23]. This conclusion is reached by using a simple DBS model applied to realistic gyrokinetic simulations. We show that the separable turbulence spectra (Gaussian, top hat, Lorentzian, etc.) used in previous theoretical and modelling works [33, 41, 42, 47, 60, 62, 97, 98] do not contain the variation of $l_r(k_{b0})$ with k_{b0}. For those turbulence spectra, the average correlation length is equal to the scale-dependent correlation length by construction, $l_r^{\text{avg}} = l_r(k_{b0})$, which may be the reason why this has not been emphasized in the literature until now. This is an important realization for interpreting RCDR measurements and for potential future cross-diagnostic comparisons. An analytical expression for the density fluctuation turbulence wavenumber spectrum is proposed. The use of analytic, nonseparable power law spectra to model magnetized plasma turbulence in tokamaks is not new (see, for example, [110]), but it is new in the context of RCDR modelling. Fit to gyrokinetic simulation spectra, the proposed analytic spectrum is able to capture the dependence $l_r \propto k_b^{-\alpha}$ with $\alpha \approx 1$, exhibit a peak correlation length $l_r(k_b)$ for a finite k_b, and reasonably reproduce the eddy aspect ratio by the ratio of the spectral widths $l_r/l_b \approx w_{k_b}/w_{k_n}$. The functional shape for the spectrum (equation (7))

could be used in future studies to more accurately represent intrinsic turbulence characteristics, as well as to differentiate these from effects due to the diagnostic measurement (forward scattering).

The variation of the correlation length with the binormal wavenumber $l_r(k_b) \sim Ck_b^{-\alpha}$ ($\sim Ck_\perp^{-\alpha}$ in conventional notation, $\alpha \approx 1$) appears to be an intrinsic characteristic of the turbulence emanating from the non-separable, power law character of the turbulent spectrum (equation (7)). This is particularly true in the core of magnetic confinement fusion devices, as suggested by the ETG and ITG driven turbulence conditions analysed here. This relationship shows how the radial and binormal characteristic lengths of individual eddies vary scale by scale, and is independent of a particular Doppler backscattering measurement. This work only discusses the scale dependence of $l_r(k_b)$ with k_b obtained from local, flux tube turbulence simulations and in ITG/ETG turbulence driven regimes. However, we expect the scale dependence of $l_r(k_b)$ with k_b to characterize regimes where global effects are important, as well as in conditions where other turbulent modes are predominantly driving turbulence. The particular spectral parameters and turbulence characteristics will likely be quantitatively different (e.g. the spectral exponents, the spectral widths, the spectral peak, etc. from equation (7)), but the nonseparable, power law *character* of the turbulent spectrum (and not its specific parameter values) is expected to carry over into other turbulent regimes. This issue could be addressed in detail in future works. The dependence of l_r on k_b found here agrees with previous experimental RCDR measurements carried out at the TJ-II stellarator [109] when measuring in the linear response regime. Previous works pointed to a diagnostic effect, the poorly localized forward scattering contribution along the beam path [41, 62], as an explanation. The forward scattering contribution to the DBS signal is absent in the present DBS model, and we cannot discriminate its importance compared to the variation of the turbulent characteristics with binormal wavenumber as an explanation for the observations in [109]. The idea that the dependence of l_r on k_b may be physical has already been mentioned in [109]. Our results suggest that the variation of l_r should at least be considered important in order to quantitatively interpret RCDR measurements.

The scale-dependent correlation length is only accessible when it satisfies $l_r(k_{b0}) \gg W_n$, that is, for very small values of the radial resolution W_n. This applies to ion-scale RCDR measurements, and is consistent with the agreement between the experimental, simulated and synthetic correlation lengths obtained from low β_e, ion-scale measurements at the FT-2 tokamak [43, 44, 48]. For $W_n \gtrsim l_r(k_{b0})$, the measured l_r^{exp} becomes dominated by the radial resolution W_n. This will likely happen for electron-scale measurements. These conclusions are reached using a local model for the scattered amplitude and a Gaussian filter shape (equation (3)), which can contain a combination of beam width and phase surface curvature affecting the radial resolution. This conclusion is independent of the specific shape of the Gaussian scattering filter, and applies to other non-Gaussian filters. Additional effects such as high amplitude turbulent fluctuations at the plasma edge are expected to produce microwave beam broadening, as is the case for electron cyclotron heating and current drive microwave beams [111–122]. Accurately taking these effects into account might be necessary for a quantitative interpretation of experiments, which will require more sophisticated beam-tracing, wave-kinetic or full-wave models.

Interestingly, when $l_r(k_{b0}) \gg W_n$ and the eddy tilt angle is negligible, this work has highlighted the possibility of measuring the eddy aspect ratio in the perpendicular dimensions to the background magnetic field **B**. Since one expects $l_r \approx Ck_b^{-\alpha}$ with $\alpha \approx 1$, the aspect ratio can be approximated by $l_r/l_b \approx C\arccos(1/\mathrm{e})^{-\alpha} \approx l_r k_b/1.19$, suggesting that the eddy aspect ratio could directly be inferred from specific RCDR experiments by computing the radial correlation length by cross-correlation of the nearby DBS slave signals, and the measured k_b from ray- or beam-tracing calculations. This estimate is shown to agree with the average eddy aspect ratio computed from the $2D$ correlation function $\mathrm{CCF}_{2D}^{\mathrm{avg}}(\Delta x, \Delta y)$ (details in appendix C). However, the eddy aspect ratio can only be accurately measured when there is negligible eddy tilt in the perpendicular plane to **B**. As shown in sections 3 and 4, the background $E \times B$ shear can induce a strong eddy tilt, making it difficult to measure the aspect ratio by this method. Interestingly, both the ion- and electron-scale conditions show that the intrinsic eddy aspect ratio along the tilted axes l_r/l_b increases for finite tilt (γ_E^{exp}) with respect to the untilted case ($\gamma_E = 0$), while the radial correlation length along the physical x-direction is reduced by γ_E, as expected. Although not shown here, additional effects such as off-midplane RCDR measurements (effect of magnetic shear $\hat{s}$) and up-down asymmetric geometries are expected to induce eddy tilt [93], which should be taken into account when performing RCDR experiments. In conditions of finite eddy tilt, a combination of the estimate proposed here to characterize the eddy aspect ratio ($l_r/l_b \sim l_r k_b/1.19$) and that proposed by Pinzón *et al* to measure the eddy tilt angle [97, 98] could be used in future studies to simultaneously characterize the eddy aspect ratio and eddy tilt angle.

In this manuscript, we have strived to make the gyrokinetic simulation work easily interpretable to the experimental RCDR community by working in real-space coordinates (x, y), representing real lengths [m] in physical space. Obtaining quantitative comparisons between experimental turbulence measurements and direct numerical simulations is known to be a challenge for the validation of turbulent transport models [6–8], and the gap often lies in nontrivial geometry considerations between experimental measurements (which often operate in conventional cylindrical coordinates) and gyrokinetic simulations (which operate in field-aligned geometry). The normal x and binormal y components can be easily mapped from the internal radial and binormal components from specific gyrokinetic codes (appendix A). Interestingly, inferring the eddy aspect ratio and the eddy tilt angle (although not extensively analyzed here) using the internal field-aligned coordinates in GYRO for the NSTX case yields error factors of $\times 5-6$. This is due to the strongly shaped flux-surface geometry characteristic of spherical tokamaks, where parameters such as elongation and Shafranov's shift

can strongly deform the field-aligned flux tube at the outboard midplane. Although not as dramatically, inferring eddy tilt and aspect ratios for the JET L-mode case from the GS2 field-aligned coordinates can yield factors of ≈30%–60% error. This suggests that achieving quantitative comparisons of the eddy tilt and aspect ratio between experiments and simulation of conventional tokamaks requires carefully considering physical (x, y) coordinates (or equivalent), and not the internally defined field-aligned coordinates characteristic of gyrokinetic codes. Additional details on this discussion are provided in appendix C. A quantitative interpretation of the measured radial correlation length, eddy aspect ratio and eddy tilt angle could be used to place strict constraints on turbulence and transport models. For example, it could prove useful to untangle the differing dependences that the turbulent heat fluxes and correlation length have exhibited with the isotope mass (isotope effect) in recent gyrokinetic simulations of ITER-extrapolated scenarios [124], which could have important consequences for the projections of future devices.

The highly simplified model DBS used in this work can be derived from a first principles, linear response DBS model recently developed for beam tracing [74]. However, it has important limitations that are known to affect the response of the backscattered signal, such as the problem of localization and scattering along the beam path contributing to poorly localized forward scattering [41, 60] (we assumed a localized signal response from the cutoff), the problem of wavenumber resolution [38, 101, 102, 123] (unimportant for our discussion as long as $W_b \gg 2\pi/k_{b0}$), the effect of the mismatch angle between the incident beam wave-vector and the binormal direction of scattering [37, 74, 78] (we assumed $\theta_{\rm mis} = 0$), and multiple forward scattering yielding a nonlinear signal response to the density fluctuation amplitude (originating from high density fluctuation amplitudes [62, 108, 125–132]; we assumed a purely linear response, equation (2)), among other things. To understand these phenomena from a fundamental perspective, more sophisticated theoretical scattering models are necessary. For modelling purposes, full-wave simulations possibly yield the most accurate representation of these phenomena for direct comparisons with experimental measurements [62, 127–132]. For the purposes of transport model validation, if the question asked is whether gyrokinetic simulations can accurately represent all experimental turbulence phenomena possibly measured by Doppler backscattering (turbulent fluctuation wavenumber spectrum, radial correlation lengths, tilt angle, etc.), then arguably the most sophisticated models (full-wave) should be considered to try to *match* experimental measurements. A particular concern when using full-physics models arises when agreement between experiments and simulations is not achieved. Is it to do with the gyrokinetic simulations, which might not accurately describe the turbulent fluctuations, or is it due to some important physical mechanism contained in a highly sophisticated model of Doppler backscattering (such as full-wave simulations)? In those circumstances, it is often difficult to reach a conclusion as to what the source of disagreement might be, and it might be instructive to break the problem into small pieces. In this manuscript, we have opted to apply a bottom-up approach by considering a simple model DBS, which does *not* contain all possible physical phenomena affecting the DBS signal, but which is simple enough to understand its direct implications on DBS measurements. Arguably, it is the simplest model for the response to a single k_b originating from a finite radial region W_n. This has yielded insight into the scale-dependent correlation length that the DBS signal is sensitive to, as well as the effect of a finite W_n on the measured correlation length. More sophisticated models will contain these, and also additional effects. In future work, we will consider extending the present DBS model, in line with recent work [41, 42, 74, 108, 126], in order to account for some of the cited additional phenomena, and their implications for RCDR. These will also be useful for qualifying the predictions from the present model.

Data availability statement

The data that support the findings of this study are available upon reasonable request from the authors.

Acknowledgments

The author would like to thank the whole NSTX team for providing the profile data used for the analysis of the plasma discharge presented here. Discussions with T Estrada and D Carralero have also been insightful for the preparation of this manuscript. This work has been supported by U.S. D.O.E. Contract DE-AC02-09CH11466, and in part by the Engineering and Physical Sciences Research Council (EPSRC) [EP/R034737/1]. Computer simulations were carried out at the National Energy Research Scientific Computing Center, supported by the Office of Science of the U.S. D.O.E. under Contract No. DE-AC02-05CH11231, at the MIT-PSFC partition of the Engaging cluster at the MGHPCC facility (www.mghpcc.org), which was funded by D O E Grant No. DE-FG02-91-ER54109, and the supercomputer ARCHER in the UK, which was funded by EPSRC [EP/R034737/1]. C Holland was partially funded by U.S. D.O.E. Grant No. DE-SC0018287. This work has been carried out within the framework of the EUROfusion Consortium and has received funding from the Euratom research and training programme 2014–2018 and 2019–2020 under Grant Agreement No. 633053. The views and opinions expressed herein do not necessarily reflect those of the European Commission.

Appendix A. Definitions and normalizations in GYRO and GS2

In this appendix we include the definitions of the GYRO and GS2 internally defined wavenumber components, and their relation to the normal and binormal components (k_n, k_b) employed throughout this manuscript.

GYRO and GS2 solve the nonlinear gyrokinetic equation in a field-aligned coordinate system in which the magnetic field is written as $\mathbf{B} = \nabla\alpha \times \nabla\psi$ [133], where α is the field-line label and ψ is the poloidal flux divided by 2π. The density

fluctuation field δn is decomposed into a slowly varying part (parallel coordinate θ along the magnetic field $\mathbf{B}$) and a rapidly varying part e^{iS} ($|S| \gg 1$), $\mathrm{f}(\mathbf{r}) = \sum_{\mathbf{k}_\perp} \hat{\mathrm{f}}_{\mathbf{k}_\perp}(\theta)\mathrm{e}^{iS(\mathbf{r},\mathbf{k}_\perp)}$, where $\mathbf{k}_\perp \equiv \nabla S$ is the perpendicular wave-vector to the magnetic field $\mathbf{B}$. In what follows we describe how this representation in GYRO and GS2 is related to the (k_n, k_b) wavenumber components.

A.1. GYRO

In the case of GYRO, the eikonal function is written as $S = -n\alpha + 2\pi pr/L_r$, where r is the radial coordinate (half of the flux surface diameter for $\theta = 0$), n is the toroidal mode number, p is the radial mode number and L_r is the radial box size. The electron density fluctuation field δn is expanded as $\delta n(\mathbf{r},t) = \sum_{n,p} \delta n_{np}(\theta,t)\mathrm{e}^{-in\alpha}\mathrm{e}^{i2\pi pr/L_r}$ [67, 70]. In this work GYRO is run in the *local* approximation in which the background profiles and gradients are taken as constant. Correspondingly, the function α is considered only as a function of θ, that is, $\alpha(r,\theta) \to \alpha(r_0,\theta)$, meaning that the decomposition $\sum_{n,p}$ is equivalent to a Fourier decomposition in (n,p) (r_0 is taken as the center of the radial domain). The function α can be readily computed from knowledge of the flux-surface shape $\big(R(r,\theta), Z(r,\theta)\big)$. We use the Miller equilibrium parametrization [82].

The GYRO radial and poloidal wavenumbers are defined by $k_r = 2\pi p/L_r$ and $k_\theta = nq/r_0$ where q is the value of the safety factor at r_0. These are normalized by the ion-sound gyro-radius $\rho_{s,\mathrm{unit}} = \frac{\bar{c}_s}{eB_{\mathrm{unit}}/m_i c}$, where B_{unit} is the *effective field strength* $B_{\mathrm{unit}} = \frac{q}{r}\frac{\mathrm{d}\psi}{\mathrm{d}r}$ and $\bar{c}_s = \sqrt{\bar{T}_e/m_i}$ the sound speed evaluated at the reference radius r_0. These definitions and normalization are internal to GYRO and differ from those implemented in GS2.

A.2. GS2

GS2 uses equivalent coordinates to solve for the nonlinear gyrokinetic equation. The eikonal function in GS2 is written as $S = n(\alpha + q\theta_0) = \mathrm{x}k_\mathrm{x} + \mathrm{y}k_\mathrm{y}$, and the sum $\sum_{\mathbf{k}_\perp} = \sum_{k_\mathrm{x},k_\mathrm{y}}$ (note the different notation between the GS2 (x,y) and the real-space (x,y) employed throughout the manuscript). The field δn is expanded as $\delta n(\mathbf{r},t) = \sum_{k_\mathrm{x},k_\mathrm{y}} \delta\hat{n}(k_\mathrm{x},k_\mathrm{y},\theta,t)\mathrm{e}^{ik_\mathrm{x}\mathrm{x}}\mathrm{e}^{ik_\mathrm{y}\mathrm{y}}$, consistent with the *local*, flux tube formulation of GS2. Here k_x and k_y are the spectral radial and 'poloidal' coordinates. The center of the flux tube is at (α_0,ψ_0). The variables $\mathrm{x},\mathrm{y},k_\mathrm{x}$ and k_y are defined by $k_\mathrm{y} = \frac{n}{a}/\frac{\mathrm{d}\psi_N}{\mathrm{d}\rho}$, $k_\mathrm{x} = k_\mathrm{y}\hat{s}\theta_0$, $\mathrm{x} = a\frac{q}{\rho}(\psi_N - \psi_{N0})$, and $\mathrm{y} = a\frac{\mathrm{d}\psi_N}{\mathrm{d}\rho}(\alpha - \alpha_0)$, where a is the half diameter at the last closed flux surface (LCFS), ψ_N is the normalized poloidal flux $\psi_N = \psi/a^2B_{\mathrm{ref}}$, $\rho = r/a$ is the normalized radial coordinate at the local $\psi = \psi_0$, $\hat{s}$ is the magnetic shear, B_{ref} the reference field in GS2 and θ_0 the parameter relating k_x and k_y via $k_\mathrm{x} = k_\mathrm{y}\hat{s}\theta_0$.

The standard GS2 normalization is that wavenumbers k_x and k_y are normalized by a reference gyro-radius ρ_r, where ρ_r is defined by $\rho_r = v_{tr}/\Omega_r$, $v_{tr} = \sqrt{2T_r/m_r}$ and $\Omega_r = eB_{\mathrm{ref}}/m_r c$ (T_r is the reference temperature, m_r the reference mass, c the speed of light). In this manuscript we have chosen the deuterium ions as the reference species and B_{ref} as the on-axis toroidal magnetic field strength. This normalization differs from that employed in GYRO by the $\sqrt{2}$ in v_{tr}, the reference field B_{ref} vs. the GYRO B_{unit}, and the use of T_i for normalizations instead of T_e. In the case of GS2, we also employ the Miller flux-surface parametrization for $\big(R(r,\theta), Z(r,\theta)\big)$.

A.3. Normal and binormal components k_n and k_b

In order to reconcile the coordinate definitions in different gyrokinetic codes, throughout this manuscript we have opted to employ the normal and binormal wavenumber components k_n and k_b which are *not* dependent on a specific gyrokinetic code and carry information about real-space length scales. They correspond to real inverse lengths in physical space. These components are routinely employed in experimental measurements to characterize the measured $\mathbf{k}$ (via ray tracing, beam tracing or full-wave simulations), and provide a natural common reference with which to compare experimental measurements and gyrokinetic simulation.

The eikonal function S used to expand the field δn in a gyrokinetic simulation can be used to define the normal and binormal wavenumber components from those defined in a specific gyrokinetic code, via the relations $k_n = \mathbf{e_n}\cdot\mathbf{k}_\perp$, and $k_b = \mathbf{e_b}\cdot\mathbf{k}_\perp$ where the normal and binormal unit vectors are defined by $\mathbf{e_n} = \frac{\nabla r}{|\nabla r|}$ and $\mathbf{e_b} = \mathbf{e_n}\times\mathbf{b}$, and $\mathbf{k}_\perp = \nabla S$ ($\mathbf{b} = \mathbf{B}/|\mathbf{B}|$). In this manuscript we restrict ourselves to fluctuations taken at the outboard midplane ($\theta = 0$), which is the location where traditional drift-wave ballooning type instabilities tend to exhibit highest amplitude and where the vast majority of fluctuation measurements are performed. The components k_n and k_b take a simple form at the outboard midplane, and are related to the GYRO (k_r, k_θ) and GS2 $(k_\mathrm{x}, k_\mathrm{y})$ via:

$$
\begin{aligned}
k_n &= |\nabla r| k_r && \text{(GYRO)}\\
&= \frac{q}{\rho}\frac{\mathrm{d}\psi_N}{\mathrm{d}\rho}|\nabla r| k_\mathrm{x} && \text{(GS2)}\,,\\
k_b &= -\left[\frac{1}{R^2} + \left(\frac{\partial\alpha}{\partial\theta}\right)^2 \Big/ (r^2\kappa^2)\right]^{1/2}\frac{r}{q}k_\theta && \text{(GYRO)}\\
&= a\frac{\mathrm{d}\psi_N}{\mathrm{d}\rho}\left[\frac{1}{R^2} + \left(\frac{\partial\alpha}{\partial\theta}\right)^2 \Big/ (\rho^2 a^2\,\kappa^2)\right]^{1/2} k_\mathrm{y} && \text{(GS2)}, \qquad (9)
\end{aligned}
$$

where κ is the flux-surface elongation as defined in the Miller geometry representation. With these definitions, we can write both the GYRO and GS2 eikonal function S (at the outboard midplane) in a compact form as $S = xk_n + yk_b$, where

$$
\begin{aligned}
x &= (r - r_0)/|\nabla r| && \text{(GYRO)}\\
&= \frac{\rho}{q\frac{\mathrm{d}\psi_N}{\mathrm{d}\rho}|\nabla r|}\mathrm{x} && \text{(GS2)}\,,\\
y &= (\alpha - \alpha_0)\Big/\left[\left(\frac{\partial\alpha}{\partial\theta}\right)^2 \Big/ (r^2\,\kappa^2) + \frac{1}{R^2}\right]^{1/2} && \text{(GYRO)}\\
&= \frac{\mathrm{y}}{a\frac{\mathrm{d}\psi_N}{\mathrm{d}\rho}}\Big/\left[\left(\frac{\partial\alpha}{\partial\theta}\right)^2 \Big/ (\rho^2 a^2\,\kappa^2) + \frac{1}{R^2}\right]^{1/2} && \text{(GS2)}. \qquad (10)
\end{aligned}
$$

Both GYRO and GS2 exhibit the same parametric, physical dependences on the local flux surface geometry (terms in $|\nabla r|, \partial\alpha/\partial\theta, \kappa, \ldots$), but the expressions differ in the specific definitions and normalizations from each code (use of variable α vs. y, r vs. x, etc. …). The coordinates (x, y) [m] are the normal and binormal coordinates employed throughout this manuscript, and correspond to real lengths in physical space. Note, for example, how the radial direction in physical space is related to the field-aligned radial direction by a factor $|\nabla r|$ which contains information about the compression of the flux-surface at the outboard midplane due to Shafranov's shift. The factor in square brackets $[.]^{1/2}$ in equations (9) and (10) indicates that the binormal component at the outboard midplane is a combination of a toroidal component (term in $1/R$) and a vertical component along the Z direction (term in $\frac{\partial\alpha}{\partial\theta}/(r\kappa)$ at the outboard midplane). The vertical component exhibits a dependence on κ, showing how elongation affects the vertical dimension via the stretching of the flux surface at the outboard midplane.

Using these definitions, equation (2) is written using $\delta\hat{n}(\mathbf{k}_\perp, \theta, t) = \delta n_{np}(\theta, t)$ in the case of GYRO, while $\delta\hat{n}(\mathbf{k}_\perp, \theta, t) = \delta\hat{n}_{k_x,k_y}(\theta, t)$ in the case of GS2. The mappings in equations (9) and (10) are employed throughout the manuscript to compute the wavenumber components (k_n, k_b) and the real-space coordinates (x, y) from the internal GYRO and GS2 definitions. As mentioned in the main text, at the outboard midplane of an up-down symmetric flux surface $k_n \propto k_r$ (GYRO) $\propto k_x$ (GS2) and $k_b \propto k_\theta$ (GYRO) $\propto k_y$ (GS2). This has allowed the expansion $e^{ik_n x + ik_b y}$ in equation (1) (a more complicated form would have been necessary for $\theta \neq 0$). For completeness, the general mapping between the GYRO and GS2 wavenumbers and k_n and k_b at arbitrary poloidal location θ is:

$$\begin{cases} k_n = -n\dfrac{\nabla\alpha\cdot\nabla r}{|\nabla r|} + \dfrac{2\pi p}{L_r}|\nabla r| \,, \\ k_b = n\left(\mathbf{b}\times\dfrac{\nabla r}{|\nabla r|}\right)\cdot\nabla\alpha \,, \end{cases} \quad \text{(GYRO)}, \qquad (11)$$

$$\begin{cases} k_n = a\dfrac{\mathrm{d}\psi_N}{\mathrm{d}\rho}\dfrac{\nabla\alpha\cdot\nabla r}{|\nabla r|}k_y + \dfrac{q}{\rho}\dfrac{\mathrm{d}\psi_N}{\mathrm{d}\rho}|\nabla r|k_x \,, \\ k_b = -a\dfrac{\mathrm{d}\psi_N}{\mathrm{d}\rho}\left(\mathbf{b}\times\dfrac{\nabla r}{|\nabla r|}\right)\cdot\nabla\alpha\, k_y, \end{cases} \quad \text{(GS2)} \quad (12)$$

which reduces to equation (9) for $\theta = 0$. As a side note, equations (9), (11) and (12) show that the GYRO (k_r, k_θ) components are related to the GS2 (k_x, k_y) by $k_r = \frac{q}{\rho}\frac{\mathrm{d}\psi_N}{\mathrm{d}\rho}k_x$ and $k_\theta = -\frac{q}{\rho}\frac{\mathrm{d}\psi_N}{\mathrm{d}\rho}k_y$, where the constant of proportionality is simply $B_{\text{unit}}/B_{\text{ref}}$.

This discussion has focused on technical details without making any assessment of the impact on the real measurement. Appendix C discusses the important consequences of using the real space coordinates for interpreting experimental measurements and performing quantitative comparisons.

Appendix B. Definitions of the radial correlation function

In this appendix we include the details needed to calculate the cross-correlation functions employed throughout this manuscript (equations (4)). The average turbulence radial correlation function $\mathrm{CCF}^{\mathrm{avg}}$ is defined as:

$$\begin{aligned} \mathrm{CCF}^{\mathrm{avg}}(\Delta x) &= \frac{\langle\delta n(x_0+\Delta x, y_0)\delta n(x_0, y_0)\rangle_{x_0,y_0,T}}{\langle|\delta n(x_0, y_0)|^2\rangle_{x_0,y_0,T}} \\ &= \frac{\int_T \mathrm{d}t \int \mathrm{d}x_0 \int \mathrm{d}y_0 \; \delta n(\mathbf{r_0} + \Delta x\mathbf{e_n})\delta n(\mathbf{r_0})}{\int_T \mathrm{d}t \int \mathrm{d}x_0 \int \mathrm{d}y_0 \; |\delta n(\mathbf{r_0})|^2} \\ &= \frac{\sum_{k_n,k_b}\langle|\delta\hat{n}(k_n,k_b)|^2\rangle_T \, e^{ik_n\Delta x}}{\sum_{k_n,k_b}\langle|\delta\hat{n}(k_n,k_b)|^2\rangle_T}, \end{aligned} \qquad (13)$$

where $\mathbf{r_0} = (x_0, y_0, \theta = 0)$, $\delta n(\mathbf{r_0})$ is expanded following equation (1), and the time variable t was omitted for clarity. The integration $\mathrm{d}x_0$, $\mathrm{d}y_0$ and $\mathrm{d}t$ is equivalent in this model to an ensemble average, since essentially any (x, y) location within a local flux tube and turbulence realization at a time t should give rise to the same turbulent fluctuations statistically. Expression (13) also shows how the radial correlation function of the turbulence is the Fourier transform of the time averaged density fluctuation power spectrum. This remains valid for the subsequent correlation functions. Note the normalization ensures $\mathrm{CCF}^{\mathrm{avg}} = 1$ for $\Delta x = 0$. The correlation length from equation (13) is represented in figures 3, 5, 6 and 8 as a horizontal dashed line.

A generalization of $\mathrm{CCF}^{\mathrm{avg}}$ is the 2D correlation function in Δx and Δy, briefly introduced in the main body of the text to discuss 2D turbulence properties such as the eddy aspect ratio and eddy tilt. It is defined as:

$$\begin{aligned} &\mathrm{CCF}^{\mathrm{avg}}_{2D}(\Delta x, \Delta y) \\ &= \frac{\langle\delta n(x_0+\Delta x, y_0+\Delta y)\delta n(x_0, y_0)\rangle_{x_0,y_0,T}}{\langle|\delta n(x_0, y_0)|^2\rangle_{x_0,y_0,T}} \\ &= \frac{\int_T \mathrm{d}t \int \mathrm{d}x_0 \int \mathrm{d}y_0 \; \delta n(\mathbf{r_0} + \Delta x\mathbf{e_n} + \Delta y\mathbf{e_b})\delta n(\mathbf{r_0})}{\int_T \mathrm{d}t \int \mathrm{d}x_0 \int \mathrm{d}y_0 \; |\delta n(\mathbf{r_0})|^2} \\ &= \frac{\sum_{k_n,k_b}\langle|\delta\hat{n}(k_n,k_b)|^2\rangle_T \, e^{ik_n\Delta x}e^{ik_b\Delta y}}{\sum_{k_n,k_b}\langle|\delta\hat{n}(k_n,k_b)|^2\rangle_T}. \end{aligned} \qquad (14)$$

Equation (14) is represented in figures 4 and 7 of the main body of the text. Note the sum over k_b in equation (14), which represents the sum over scales and motivates the denomination of the 2D *average* correlation function of the turbulence. By extension, the 2D scale-dependent correlation function for binormal wavenumber k_b, $\mathrm{CCF}^{k_b}_{2D}$, is calculated by removing the $\sum_{k_b}$ and replacing the quantity under the summatory sign with the specific desired k_b. This leads to a cosinusoidal dependence of $\mathrm{CCF}^{k_b}_{2D}$ in the Δy direction, while only the sum over k_n remains, giving

$$\mathrm{CCF}^{k_b}_{2D}(\Delta x, \Delta y) = \cos(k_b\Delta y)\frac{\sum_{k_n}\langle|\delta\hat{n}(k_n,k_b)|^2\rangle_T \, e^{ik_n\Delta x}}{\sum_{k_n}\langle|\delta\hat{n}(k_n,k_b)|^2\rangle_T}. \qquad (15)$$

This expression is used in sections 3.1 and 4.1 to compute the binormal correlation length l_b as the 1/e value of $\mathrm{CCF}^{k_b}_{2D}$ for $\Delta x = 0$, that is $\mathrm{CCF}^{k_b}_{2D}(\Delta x = 0, l_b) = 1/\mathrm{e}$, giving the quoted value $l_b = \arccos(1/\mathrm{e})/k_b$. The 1D scale-dependent correlation function CCF^{k_b} and the synthetic correlation functions $\mathrm{CCF}^{\mathrm{syn}}$ are defined as

$$\begin{aligned}
\mathrm{CCF}^{k_b}(\Delta x) &= \frac{\langle \delta\tilde{n}(x_0+\Delta x, k_b)\delta\tilde{n}(x_0,k_b)^*\rangle_{x_0,T}}{\langle|\delta\hat{n}(x_0,k_b)|^2\rangle_{x_0,T}} \\
&= \frac{\sum_{k_n}\langle|\delta\hat{n}(k_n,k_b)|^2\rangle_T\, \mathrm{e}^{ik_n\Delta x}}{\sum_{k_n}\langle|\delta\hat{n}(k_n,k_b)|^2\rangle_T}, \\
&\mathrm{CCF}^{\mathrm{syn}}(\Delta x) \\
&= \frac{\langle A_s(\mathbf{r_0}+\Delta x\mathbf{e_n}, k_{b0}\mathbf{e_b})A_s(\mathbf{r_0},k_{b0}\mathbf{e_b})^*\rangle_{x_0,y_0,T}}{\langle|A_s(\mathbf{r_0},k_{b0}\mathbf{e_b})|^2\rangle_{x_0,y_0,T}} \\
&= \frac{\sum_{k_n,k_b}\mathrm{e}^{-k_n^2W_n^2/2}\mathrm{e}^{-(k_b-k_{b0})^2W_b^2/2}\langle|\delta\hat{n}(k_n,k_b)|^2\rangle_T\,\mathrm{e}^{ik_n\Delta x}}{\sum_{k_n,k_b}\mathrm{e}^{-k_n^2W_n^2/2}\mathrm{e}^{-(k_b-k_{b0})^2W_b^2/2}\langle|\delta\hat{n}(k_n,k_b)|^2\rangle_T},
\end{aligned} \tag{16}$$

which agree with the expressions used in equation (5). In equation (16), $\delta\tilde{n}$ is Fourier decomposed in y but not in x, while $\delta\hat{n}$ is Fourier decomposed in both x and y. Note that the computation of CCF^{k_b} only requires a sum over k_n, since by definition the k_b component is selected, while the sum is made over k_n and k_b in $\mathrm{CCF}^{\mathrm{avg}}$ and $\mathrm{CCF}^{\mathrm{syn}}$. For the experimentally relevant values $W_b \gg 2\pi/k_{b0}$, we have:

$$\mathrm{CCF}^{\mathrm{syn}}(\Delta x) \to \frac{\sum_{k_n}\mathrm{e}^{-k_n^2W_n^2/2}\langle|\delta\hat{n}(k_n,k_{b0})|^2\rangle_T\,\mathrm{e}^{ik_n\Delta x}}{\sum_{k_n}\mathrm{e}^{-k_n^2W_n^2/2}\langle|\delta\hat{n}(k_n,k_{b0})|^2\rangle_T}$$

for

$$W_b \gg 2\pi/k_{b0}. \tag{17}$$

Equation (16) shows how the synthetic correlation function is in fact a convolution product between a filter $|W(\mathbf{k}_\perp - \mathbf{k_0})|^2 = \mathrm{e}^{-k_n^2W_n^2/2}\mathrm{e}^{-(k_b-k_{b0})^2W_b^2/2}$ (equation (3), reduced to $\mathrm{e}^{-k_n^2W_n^2/2}$ in equation (17)) and the wavenumber spectrum of fluctuations. In real space, this means that the radial structure of $\mathrm{CCF}^{\mathrm{syn}}$ will be determined by the largest length scale between the Fourier transform of the filter $\propto \mathrm{e}^{-x^2/2W_n^2}$, that is W_n, and the Fourier transform of the power spectrum, that is the scale-dependent correlation length for $k_b = k_{b0}$. This explains why for $W_n \ll l_r(k_{b0})$ we recover the scale-dependent correlation length (figures 5 and 8), while for $W_n \gg l_r(k_{b0})$, the dominant scale will be $\approx W_n$.

Appendix C. Physical radial correlation length, eddy aspect ratio and eddy tilt

In this appendix we discuss some geometric considerations to take into account when interpreting the physical radial correlation length, eddy aspect ratio and tilt angle in the perpendicular direction to **B** from local flux tube gyrokinetic simulation outputs. We focus on the outboard midplane location $\theta = 0$, and intend to provide intuition behind the mathematical mappings introduced in appendix A (equations (9) and (10))[10].

Figure 12 shows the electron-scale electron density fluctuation amplitude δn and the average correlation function $\mathrm{CCF}^{\mathrm{avg}}$ as a function of the internal field-aligned coordinates (noted Δx^{sim} and Δy^{sim} here in (a) and (c)) corresponding to the electron-scale, ETG-driven turbulence condition in NSTX (section 3). These are plotted as a function of $\rho_{s,\mathrm{unit}}$, internally defined in GYRO [67, 70]. The same quantities are plotted in the real physical coordinates $(\Delta x, \Delta y)$ employed throughout this manuscript, representing real lengths [m], in (b) and (d). These are normalized to the local ρ_s. A square aspect ratio simulation domain in $(\Delta x, \Delta y)^{\mathrm{sim}}$ is compressed and stretched in real physical space owing to the highly shaped flux surface geometry characteristic of spherical tokamaks. The mapping from the simulation field-aligned $(\Delta x^{\mathrm{sim}}, \Delta y^{\mathrm{sim}})$ to the physical $(\Delta x, \Delta y)$ is made using equation (10).

In the radial direction, the Shafranov's shift measured via the $|\nabla r|$ coefficient contributes to the compression of the flux surfaces in physical space. Additionally, the $\rho_{s,\mathrm{unit}}$ value employed internally in GYRO can substantially differ from the local ρ_s ($B_{\mathrm{unit}}/B \approx 3.61$, table 1), implying a further size 'reduction' in $\Delta x/\rho_s$ with respect to $\Delta x^{\mathrm{sim}}/\rho_{s,\mathrm{unit}}$. Both factors contribute to a factor of 5–6 reduction in the physical radial domain with respect to the simulation radial domain. In the binormal direction, figure 12 does not show a substantial difference between $\Delta y^{\mathrm{sim}}/\rho_{s,\mathrm{unit}}$ and $\Delta y/\rho_s$ due to a combination of cancelling effects. The flux-surface elongation κ contributes to stretching the real domain in the vertical direction, while the $1/R^2$ term represents the toroidal component of the binormal direction (along $\mathbf{e_b}$), further contributing to the stretching of the real domain in the binormal direction Δy with respect to the simulation Δy^{sim}. These factors contributing to the stretching are counteracted by the differing ρ_s definition, which 'reduces' the domain in physical space as previously described. Overall, the difference between the simulation $\Delta y^{\mathrm{sim}}/\rho_{s,\mathrm{unit}}$ and physical $\Delta y/\rho_s$ is not substantial.

The previous discussion is pertinent when interpreting physical radial correlation lengths, aspect ratio and tilt angle from local flux tube gyrokinetic simulations. For comparisons to experiments, a factor of ≈3–4 error can be made in the radial correlation length if directly comparing to the field-aligned $(\Delta x^{\mathrm{sim}}, \Delta y^{\mathrm{sim}})$. Inferring the eddy tilt from the flux tube $(\Delta x^{\mathrm{sim}}, \Delta y^{\mathrm{sim}})$ would result in $\theta_{\mathrm{tilt}} \approx 11°$, while the physical tilt angle is $\theta_{\mathrm{tilt}} \approx 50°$, a factor $\approx \times 5$ larger. The inferred eddy aspect ratio does also greatly differ between the field-aligned $(\Delta x^{\mathrm{sim}}, \Delta y^{\mathrm{sim}})$ and real space. In particular, the cases with $\gamma_E = 0$ (zero tilt angle) exhibit an aspect ratio $l_r/l_b \approx 9$ in the field-line coordinates, while the physical aspect ratio is $l_r/l_b \approx 1.54$.

The same care needs to be taken when considering conventional tokamak flux-surface geometry such as in the JET ion-scale conditions analyzed here, although one does not

[10] A general flux tube cross section perpendicular to **B** would be twisted for finite finite shear $\hat{s}$ compared to the $\theta = 0$ cross section. This effect is not considered here.

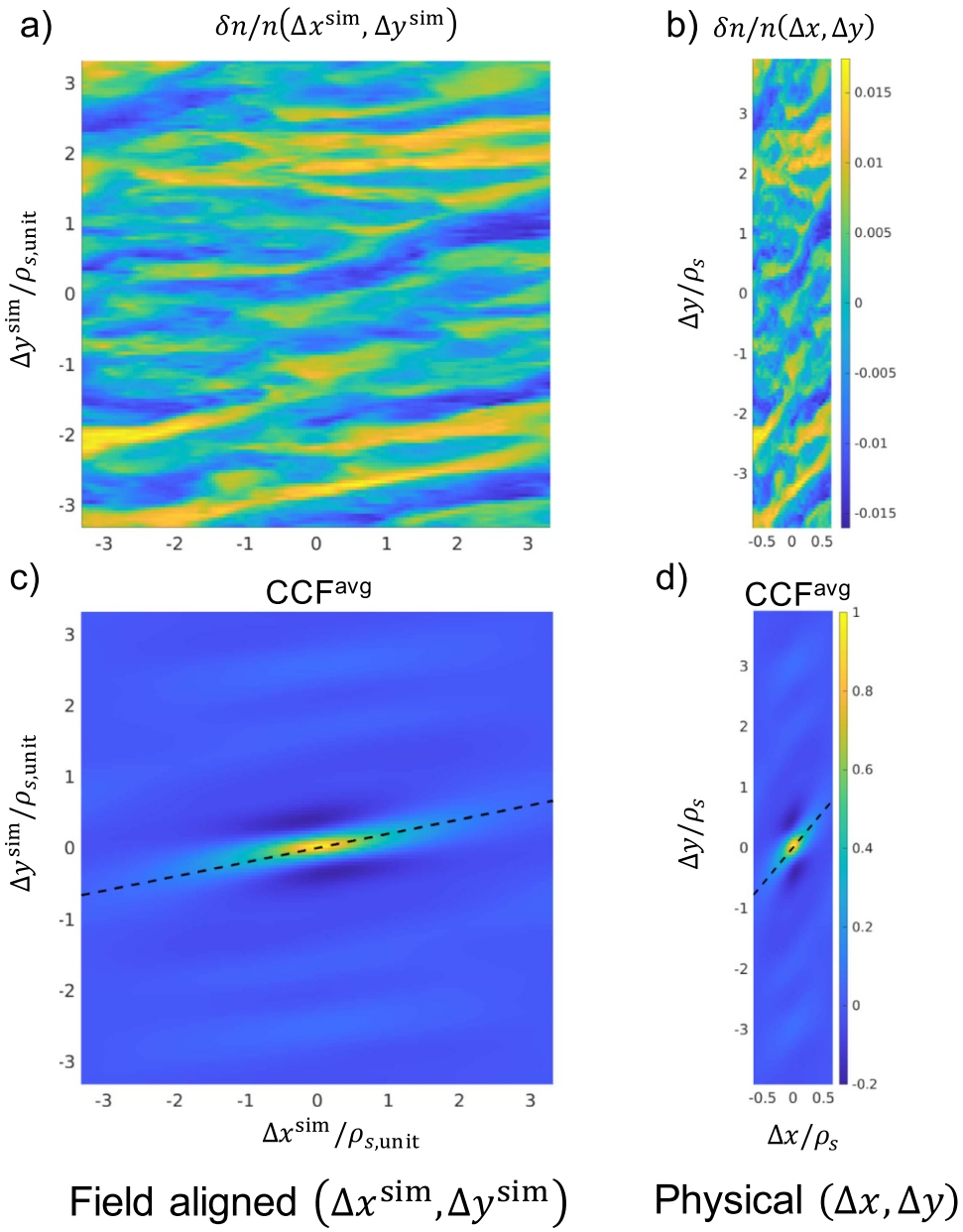

Figure 12. Comparison of the electron density fluctuation amplitude δn and the average correlation function CCF$^{\mathrm{avg}}$ as a function of the internal field-aligned coordinates (noted Δx^{sim} and Δy^{sim} here in (a) and (c)) corresponding to the electron-scale, ETG-driven turbulence condition in NSTX (section 3). To be consistent, these are plotted as a function of $\rho_{s,\mathrm{unit}}$, internally defined in GYRO [67, 70]. The same quantities are plotted in real physical coordinates $(\Delta x, \Delta y)$, representing real lengths [m], in (b) and (d), at the outboard midplane. As in the rest of the manuscript, these are normalized to the local ρ_s. Note a square aspect ratio simulation domain in $(\Delta x, \Delta y)^{\mathrm{sim}}$ is deformed in real physical space at the outboard midplane in highly shaped ST geometry.

Table 1. Local geometry parameters at the outboard midplane ($\theta = 0$) necessary for mapping the gyrokinetic simulation perpendicular domain $(\Delta x^{\mathrm{sim}}, \Delta y^{\mathrm{sim}})$ to the real space $(\Delta x, \Delta y)$.

	$\lvert\nabla r\rvert$	$\frac{\partial \alpha}{\partial \theta}$	κ	$R_0/a, R_{\mathrm{ref}}/a$	q	r/a	B
NSTX: e- scale	1.43	1.33	2.11	1.52	3.79	0.71	$B_{\mathrm{unit}}/B \approx 3.61$
JET: ion scale	1.12	1.02	1.36	3.35	1.43	0.51	$B_{\mathrm{ref}}/B \approx 1.09$, $\frac{\mathrm{d}\psi_N}{\mathrm{d}\rho} \approx 0.51$

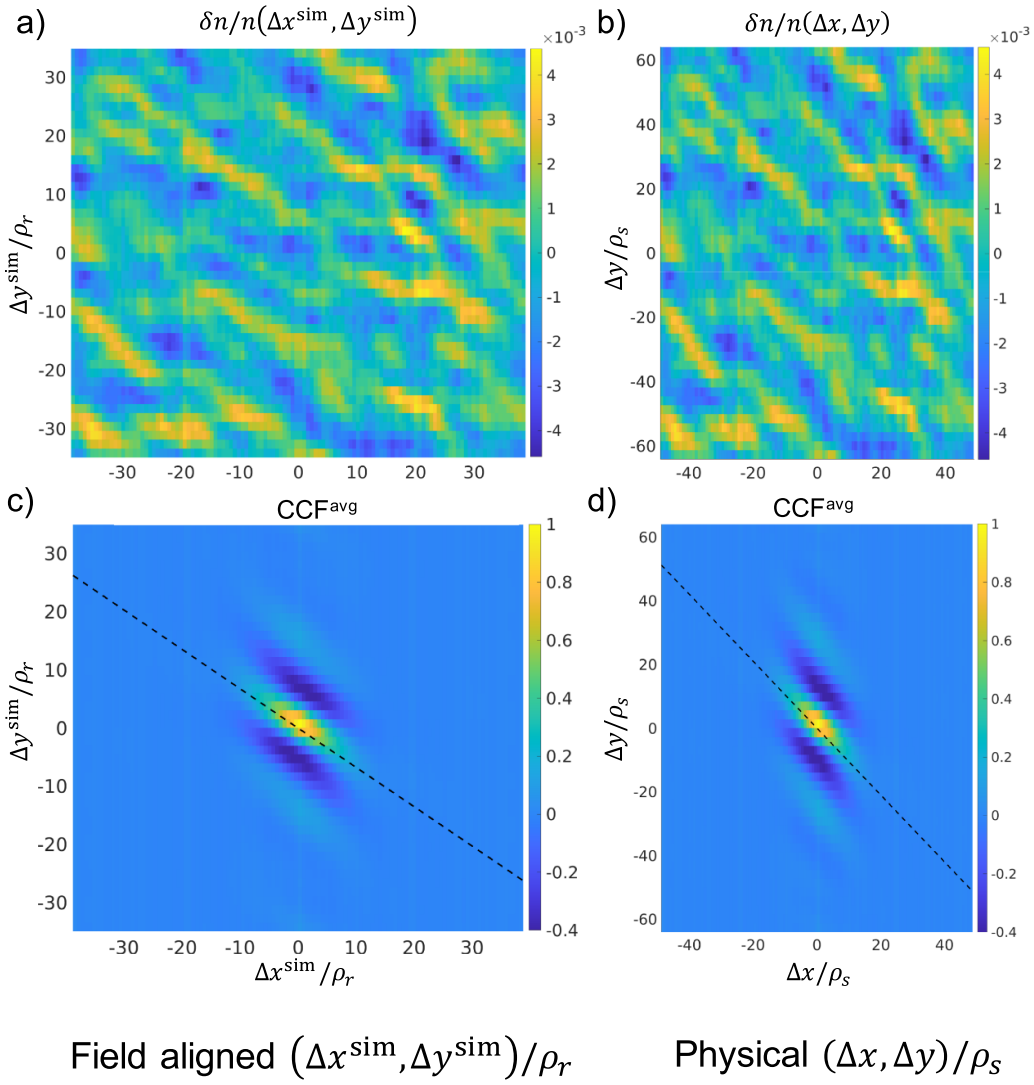

Figure 13. Comparison of the electron density fluctuation amplitude δn and the average correlation function CCF$^{\rm avg}$ as a function of the internal field-aligned coordinates (noted $\Delta x^{\rm sim}$ and $\Delta y^{\rm sim}$ here in (a) and (c), and normalized by the GS2 internally defined ρ_r) corresponding to the ion-scale, ITG-driven turbulence condition in JET (section 4). The same quantities are plotted in real physical coordinates $(\Delta x,\Delta y)$, representing real lengths [m], in (b) and (d), and normalized by the local ρ_s at the outboard midplane. In this conventional tokamak core condition, the simulation domain in $(\Delta x,\Delta y)^{\rm sim}$ is deformed when mapped to real space, but not as dramatically as the previous ST case. $\delta n/n$ is internally normalized by a/ρ_r is GS2, but not in GYRO. Here the internal GS2 fluctuation amplitude is rescaled to obtain the absolute $\delta n/n$.

expect differences as large as in the NSTX case with higher shaping. Figure 13 shows 2D plots of the density fluctuation amplitude δn and the 2D average correlation function CCF$^{\rm avg}$ corresponding to the JET ion-scale, ITG-driven condition. Visually the difference is less dramatic than in figure 12. Quantitatively, the eddy tilt calculated in the simulation $(\Delta x,\Delta y)^{\rm sim}$ would yield $\theta_{\rm tilt}\approx -32.6°$, while in physical space one finds $\theta_{\rm tilt}\approx -42.9°$. In these cases, the aspect ratio l_r/l_b is only moderately modified by $\approx 10\%$ when calculated in physical space vs. in field-aligned coordinates when $\gamma_E^{\rm exp}$ is finite, but can change by factors of $\approx 60\%$ when $\gamma_E = 0$ as we noted in the main text ($l_r/l_b \approx 2.99$ in the field-aligned frame while the physical $l_r/l_b \approx 1.88$). The geometric considerations discussed in this appendix are important when comparing the output of local flux tube gyrokinetic simulations to experimental measurements.

ORCID iDs

J Ruiz Ruiz https://orcid.org/0000-0003-4258-5273
V H Hall-Chen https://orcid.org/0000-0001-6009-3649
M Barnes https://orcid.org/0000-0002-0177-1689
J Candy https://orcid.org/0000-0003-3884-6485
J Garcia https://orcid.org/0000-0003-0900-5564
W Guttenfelder https://orcid.org/0000-0001-8181-058X
C Holland https://orcid.org/0000-0001-6029-2306
N T Howard https://orcid.org/0000-0002-8787-6309

References

[1] Liewer P C 1985 *Nucl. Fusion* **25** 5
[2] Tynan G R, Fujisawa A and McKee G 2009 *Plasma Phys. Control. Fusion* **51** 113001
[3] Horton W 1999 *Rev. Mod. Phys.* **71** 3
[4] Garbet X 2001 *Plasma Phys. Control. Fusion* **43** A251
[5] Candy J and Waltz R E 2003 *Phys. Rev. Lett.* **91** 045001
[6] Terry P W *et al* 2008 *Phys. Plasmas* **15** 062503
[7] Greenwald M 2010 *Phys. Plasmas* **17** 058101
[8] Holland C 2016 *Phys. Plasmas* **23** 060901
[9] Fonck R J, Duperrex P A and Paul S F 1990 *Rev. Sci. Instrum.* **61** 3487
[10] Fonck R J, Cosby G, Durst R D, Paul S F, Bretz N, Scott S, Synakowski E and Taylor G 1993 *Phys. Rev. Lett.* **70** 3736
[11] McKee G R *et al* 2001 *Nucl. Fusion* **41** 1235
[12] Weisen H 1988 *Rev. Sci. Instrum.* **59** 1544
[13] Coda S, Porkolab M and Carlstrom T N 1992 *Rev. Sci. Instrum.* **63** 4974
[14] Coda S and Porkolab M 1995 *Rev. Sci. Instrum.* **66** 454
[15] Coda S, Porkolab M and Burrell K H 2001 *Phys. Rev. Lett.* **86** 4835
[16] Porkolab M, Rost J C, Basse N, Dorris J, Edlund E, Lin L, Lin Y and Wukitch S 2006 *IEEE Trans. Plasma Sci.* **34** 229
[17] Cima G, Bravenec R V, Wootton A J, Rempel T D, Gandy R F, Watts C and Kwon M 1995 *Phys. Plasmas* **2** 720
[18] Sattler S and Hartfuss H J (W7-AS Team) 1994 *Phys. Rev. Lett.* **72** 653
[19] White A E *et al* 2008 *Phys. Plasmas* **15** 056116
[20] Cripwell P, Costley A E and Hubbard A E 1989 *Proc. 16th Conf. on Controlled Fusion and Plasma Physics, Venice, 1989* (*Petit-Lancy, Switzerland*) vol 13B, ed S Segre, H Knoepfel and E Sindoni (European Physical Society) p 75
[21] Costley A E, Cripwell P, Prentice R and Sips A C C 1990 *Rev. Sci. Instrum.* **61** 2823
[22] Nazikian R and Mazzucato E 1995 *Rev. Sci. Instrum.* **66** 392
[23] Nazikian R, Kramer G J and Valeo E 2001 *Phys. Plasmas* **8** 1840
[24] Rhodes T L *et al* 2002 *Phys. Plasmas* **9** 2141
[25] Hanson G R, Wilgen J B, Anabitarte E, Bell J D, Harris J H, Dunlap J L and Thomas C E 1990 *Rev. Sci. Instrum.* **61** 3049
[26] Mazzucato E and Nazikinan R 1993 *Phys. Rev. Lett.* **71** 1840
[27] Rhodes T L, Peebles W A and Doyle E J 1992 *Rev. Sci. Instrum.* **63** 4661
[28] Sanchez J, Brañas B, de la Luna E and Estrada T 1993 *Rev. Sci. Instrum.* **64** 487
[29] Conway G D 1997 *Plasma Phys. Control. Fusion* **39** 407
[30] Hutchinson I H 1992 *Plasma Phys. Control. Fusion* **34** 1225
[31] Gusakov E Z and Yu Popov A 2004 *Plasma Phys. Control. Fusion* **46** 1393
[32] Gusakov E Z and Yakovlev B O 2002 *Plasma Phys. Control. Fusion* **44** 2525
[33] Schirmer J, Conway G D, Holzhauer E, Suttrop W and Zohm H (The ASDEX Upgrade Team) 2007 *Plasma Phys. Control. Fusion* **49** 1019
[34] Holzhauer E, Hirsch M, Grossmann T, Brañas B and Serra F 1998 *Plasma Phys. Control. Fusion* **40** 1869
[35] Hirsch M, Holzhauer E, Baldzuhn J and Kurzan B 2001 *Rev. Sci. Instrum.* **72** 324
[36] Hennequin P, Honoré C, Truc A, Quéméneur A, Fenzi-Bonizec C, Bourdelle C, Garbet X and Hoang G T (The Tore Supra Team) 2006 *Nucl. Fusion* **46** S771
[37] Hillesheim J C, Crocker N A, Peebles W A, Meyer H, Meakins A, Field A R, Dunai D, Carr M and Hawkes N (The MAST Team) 2015 *Nucl. Fusion* **55** 073024
[38] Hirsch M and Holzhauer E 2004 *Plasma Phys. Control. Fusion* **46** 593
[39] Hennequin P, Honoré C, Truc A, Quéméneur A, Lemoine N, Chareau J-M and Sabot R 2004 *Rev. Sci. Instrum.* **75** 3881
[40] Hillesheim J C, Delabie E, Meyer H, Maggi C F, Meneses L and Poli E (JET Contributors) 2016 *Phys. Rev. Lett.* **116** 065002
[41] Gusakov E, Irzak M and Popov A 2014 *Plasma Phys. Control. Fusion* **56** 025009
[42] Gusakov E Z, Irzak M A, Popov A Y, Khitrov S A and Teplova N V 2017 *Phys. Plasmas* **24** 022119
[43] Gusakov E *et al* 2013 *Plasma Phys. Control. Fusion* **55** 124034
[44] Altukhov A B *et al* 2016 *Plasma Phys. Control. Fusion* **58** 105004
[45] Altukhov A B, Gurchenko A D, Gusakov E Z, Irzak M A, Niskala P, Esipov L A, Kiviniemi T P and Leerink S 2018 *Phys. Plasmas* **25** 082305
[46] Altukhov A B, Gurchenko A D, Gusakov E Z, Irzak M A, Niskala P, Esipov L A, Kiviniemi T P, Krutkin O L and Leerink S 2018 *Phys. Plasmas* **25** 112503
[47] Prisiazhniuk D, Conway G D, Krämer-Flecken A and Stroth U (The ASDEX Upgrade Team) 2018 *Plasma Phys. Control. Fusion* **60** 075003
[48] Krutkin O L *et al* 2019 *Nucl. Fusion* **59** 096017
[49] Happel T, Estrada T, Blanco E, Hidalgo C, Conway G D and Stroth U (TJ-II Team) 2011 *Phys. Plasmas* **18** 102302
[50] Conway G D, Schirmer J, Klenge S, Suttrop W and Holzhauer E (The ASDEX Upgrade Team) 2004 *Plasma Phys. Control. Fusion* **46** 951
[51] Hillesheim J C, Parra F I, Barnes M, Crocker N A, Meyer H, Peebles W A, Scannell R and Thornton A (The MAST Team) 2015 *Nucl. Fusion* **55** 032003
[52] Bourdelle C *et al* 2011 *Nucl. Fusion* **51** 063037
[53] de Meijere C A *et al* 2014 *Plasma Phys. Control. Fusion* **56** 072001
[54] Casati A *et al* 2009 *Phys. Rev. Lett.* **102** 165005
[55] Windisch T *et al* 2018 *Rev. Sci. Instrum.* **89** 10H115
[56] DeBoo J C *et al* 2010 *Phys. Plasmas* **17** 056105
[57] Silva C, Hillesheim J C, Gil L, Hidalgo C, Meneses L and Rimini F (JET Contributors) 2018 *Plasma Phys. Control. Fusion* **60** 085006
[58] Silva C, Hillesheim J C, Gil L, Hidalgo C, Maggi C F, Meneses L and Solano E R (JET Contributors) 2019 *Plasma Phys. Control. Fusion* **61** 075007
[59] Conway G D, Stegmeir A, Poli E and Strumberger E 2011 *Proc. 10th Int. Reflectometry Workshop– IRW10 (Padova)*
[60] Gusakov E Z and Surkov A V 2004 *Plasma Phys. Control. Fusion* **46** 1143
[61] Gusakov E Z and Popov A Y 2011 *Proc. 38th Conf. on Plasma Physics (Strasbourg, 27 June–1 July)* P4.056
[62] Blanco E and Estrada T 2013 *Plasma Phys. Control. Fusion* **55** 125006
[63] Ruiz Ruiz J *et al* 2015 *Phys. Plasmas* **22** 122501
[64] Ruiz Ruiz J *et al* 2019 *Plasma Phys. Control. Fusion* **61** 115015
[65] Ruiz Ruiz J, Guttenfelder W, White A E, Howard N T, Candy J, Ren Y, Smith D R and Holland C 2020 *Plasma Phys. Control. Fusion* **62** 075001
[66] Ren Y *et al* 2020 *Nucl. Fusion* **60** 026005
[67] Candy J and Waltz R E 2003 *J. Comput. Phys.* **186** 545
[68] Kotschenreuther M *et al* 1995 *Comput. Phys. Commun.* **88** 128
[69] Ruiz Ruiz J, Guttenfelder W, White A E, Howard N T, Candy J, Ren Y, Smith D R and Holland C 2020 *Phys. Plasmas* **27** 122505
[70] Candy J and Belli E 2011 *GYRO Technical Guide* General Atomics Technical Report GA-A26818

[71] Christen N, Barnes M and Parra F 2021 *J. Plasma Phys.* **87** 905870230
[72] Christen N, Barnes M, Hardman M R and Schekochihin A A 2021 arXiv:2109.07757
[73] Sugama H and Horton W 1998 *Phys. Plasmas* **5** 2560
[74] Hall-Chen V H *et al* 2022 *Plasma Phys. Control. Fusion* in press (https://doi.org/10.1088/1361-6587/ac57a1)
[75] Holland C, White A E, McKee G R, Shafer M W, Candy J, Waltz R E, Schmitz L and Tynan G R 2009 *Phys. Plasmas* **16** 052301
[76] Holland C *et al* 2012 *Nucl. Fusion* **52** 063028
[77] Hillesheim J C, Holland C, Schmitz L, Kubota S, Rhodes T L and Carter T A 2012 *Rev. Sci. Instrum.* **83** 10E331
[78] Rhodes T L, Peebles W A, Nguyen X, VanZeeland M A, deGrassie J S, Doyle E J, Wang G and Zeng L 2006 *Rev. Sci. Instrum.* **77** 10E922
[79] Belli E A and Candy J 2008 *Plasma Phys. Control. Fusion* **50** 095010
[80] Hawryluk R J 1980 An empirical approach to tokamak transport *Physics of Plasmas Close to Thermonuclear Conditions* ed B Coppi *et al* (CEC, Brussels) Vol 1 pp 19–46
[81] Guttenfelder W *et al* 2013 *Nucl. Fusion* **53** 093022
[82] Miller R L Chu M S, Greene J M, Lin-Liu Y R and Waltz R E 1998 *Phys. Plasmas* **5** 973
[83] Drake J F, Guzdar P N and Hassam A B 1988 *Phys. Rev. Lett* **61** 2205 (https://journals.aps.org/prl/abstract/10.1103/PhysRevLett.61.2205)
[84] Dorland W, Jenko F, Kotschenreuther M and Rogers B N 2000 *Phys. Rev. Lett.* **85** 5579
[85] Jenko F, Dorland W, Kotschenreuther M and Rogers B N 2000 *Phys. Plasmas* **7** 1904
[86] Roach C M *et al* 2005 *Plasma Phys. Control. Fusion* **47** B323
[87] Roach C M *et al* 2009 *Plasma Phys. Control. Fusion* **51** 124020
[88] Guttenfelder W and Candy J 2011 *Phys. Plasmas* **18** 022506
[89] Nevins W M *et al* 2006 *Phys. Plasmas* **13** 122306
[90] Jenko F and Kendl A 2002 *Phys. Plasmas* **9** 4103
[91] Biglari H, Diamond P H and Terry P W 1990 *Phys. Fluids* B **2** 1
[92] Burrell K H 1997 *Phys. Plasmas* **4** 1499
[93] Parra F I, Barnes M and Peeters A G 2011 *Phys. Plasmas* **18** 062501
[94] Shafer M W, Fonck R J, McKee G R, Holland C, White A E and Schlossberg D J 2012 *Phys. Plasmas* **19** 032504
[95] Fox M F J, van Wyk F, Field A R, Ghim Y-C, Parra F I and Schekochihin A A (The MAST Team) 2017 *Plasma Phys. Control. Fusion* **59** 034002
[96] Fox M F J, Field A R, van Wyk F, Ghim Y-c, Schekochihin A A and (the MAST Team) 2017 *Plasma Phys. Control. Fusion* **59** 044008
[97] Pinzón J R, Estrada T, Happel T, Hennequin P, Blanco E and Stroth U (The ASDEX Upgrade and TJ-II Teams) 2019 *Plasma Phys. Control. Fusion* **61** 105009
[98] Pinzón J R, Happel T, Hennequin P, Angioni C, Estrada T, Lebschy A and Stroth U (The ASDEX Upgrade Team) 2019 *Nucl. Fusion* **59** 074002
[99] Maj O, Pereverzev G V and Poli E 2009 *Phys. Plasmas* **16** 062105
[100] Maj O, Balakin A A and Poli E 2010 *Plasma Phys. Control. Fusion* **52** 085006
[101] Conway G D, Lechte C, Fochi A and The ASDEX Upgrade Team 2015 *Proc. 12th Int. Reflectometry Workshop—IRW12 (Julich)*
[102] Conway G D, Lechte C, Poli E, Maj O and the ASDEX Upgrade Team 2019 *Proc. 14th Intl. Reflectometry Workshop—IRW14 (Lausanne)*
[103] Dimits A M 1993 *Phys. Rev.* E **48** 4070
[104] Beer M *et al* 1995 *Phys. Plasmas* **2** 2687
[105] McKee G R, Fenzi C, Fonck R J and Jakubowski M 2003 *Rev. Sci. Instrum.* **74** 2014
[106] Ghim Y-c *et al* 2013 *Phys. Rev. Lett.* **110** 145002
[107] Field A R, Dunai D, Ghim Y-c, Hill P, McMillan B, Roach C M, Saarelma S, Schekochihin A A and Zoletnik S (The MAST Team) 2014 *Plasma Phys. Control. Fusion* **56** 025012
[108] Gusakov E Z, Surkov A V and Yu Popov A 2005 *Plasma Phys. Control. Fusion* **47** 959
[109] Fernández-Marina F, Estrada T and Blanco E 2014 *Nucl. Fusion* **54** 072001
[110] Staebler G M, Waltz R E, Candy J and Kinsey J E 2013 *Phys. Rev. Lett.* **110** 055003
[111] Kirov K K, Leuterer F, Pereverzev G V, Ryter F and Suttrop W (ASDEX Upgrade Team) 2002 *Plasma Phys. Control. Fusion* **44** 2583
[112] Tsironis C, Peeters A G, Isliker H, Strintzi D, Chatziantonaki I and Vlahos2 L 2009 *Phys. Plasmas* **16** 112510
[113] Peysson Y, Decker J, Morini L and Coda S 2011 *Plasma Phys. Control. Fusion* **53** 124028
[114] Ram A K, Hizanidis K and Kominis Y 2013 *Phys. Plasmas* **20** 056110
[115] Sysoeva E V, da Silva F, Gusakov E Z, Heuraux S and Popov A 2015 *Nucl. Fusion* **55** 033016
[116] Ram A K and Hizanidis K 2016 *Phys. Plasmas* **23** 022504
[117] Brookman M W, Austin M E, Gentle K W, Petty C C, Ernst D E, Peysson Y, Decker J and Barada K 2017 *EPJ Web Conf.* **147** 03001
[118] Köhn A, Guidi L, Holzhauer E, Maj O, Poli E, Snicker A and Weber H 2018 *Plasma Phys. Control. Fusion* **60** 075006
[119] Snicker A, Poli E, Maj O, Guidi L, Köhn A, Weber H, Conway G, Henderson M and Saibene G 2018 *Nucl. Fusion* **58** 016002
[120] Chellaï O *et al* 2018 *Phys. Rev. Lett.* **120** 105001
[121] Chellaï O *et al* 2019 *Plasma Phys. Control. Fusion* **61** 014001
[122] Chellaï O *et al* 2021 *Nucl. Fusion* **61** 066011
[123] Lin Y, Nazikian R, Irby J H and Marmar E S 2001 *Plasma Phys. Control. Fusion* **43** L1
[124] Garcia J, Görler T, Jenko F and Giruzzi G 2017 *Nucl. Fusion* **57** 014007
[125] Pinzón J R, Happel T, Blanco E, Conway G D, Estrada T and Stroth U 2017 *Plasma Phys. Control. Fusion* **59** 035005
[126] Krutkin O L, Gusakov E Z, Heuraux S and Lechte C 2019 *Plasma Phys. Control. Fusion* **61** 045010
[127] Blanco E and Estrada T 2008 *Plasma Phys. Control. Fusion* **50** 095011
[128] Lechte C 2009 *IEEE Trans. Plasma Sci.* **37** 1099
[129] Stroth U *et al* 2015 *Nucl. Fusion* **55** 083027
[130] Happel T *et al* 2017 *Plasma Phys. Control. Fusion* **59** 054009
[131] Lechte C, Conway G D, Görler T and Tröster-Schmid C (The ASDEX Upgrade Team) 2017 *Plasma Phys. Control. Fusion* **59** 075006
[132] Lechte C, Conway G D, Görler T and Happel T (The ASDEX Upgrade Team) 2020 *Plasma Sci. Technol.* **22** 064006
[133] Kruskal M D and Kulsrud R M 1958 *Phys. Fluids* **1** 265